

Dynamic actin-mediated nano-scale clustering of CD44 regulates its meso-scale organization at the plasma membrane

Parijat Sil^{a,†}, Nicolas Mateos^{b,†}, Sangeeta Nath^{c,d}, Sonja Buschow^e, Carlo Manzo^f, Kenichi G. N. Suzuki^{g,h}, Takahiro Fujiwara^h, Akihiro Kusumi^{h,i}, Maria F. Garcia-Parajo^{b,j,*}, and Satyajit Mayor^{a,c,*}

^aNational Centre for Biological Sciences (NCBS), ^cInstitute of Stem Cell and Regenerative Medicine, and ^dManipal Institute of Regenerative Medicine, Manipal Academy of Higher Education, Bangalore 560065, India; ^bICFO–Institut de Ciències Fotoniques, The Barcelona Institute of Science and Technology, Barcelona 08860, Spain; ^eDepartment of Gastroenterology and Hepatology, Erasmus University Medical Center Rotterdam, Rotterdam 3015 GD Rotterdam, The Netherlands; ^fFacultat de Ciències i Tecnologia, Universitat de Vic–Universitat Central de Catalunya, Vic 08500, Spain; ^gCentre for Highly Advanced Integration of Nano and Life Sciences (G-CHAIN), Gifu University, Gifu 501-1193, Japan; ^hInstitute for Integrated Cell-Material Sciences (WPI-iCeMS), Kyoto University, Kyoto 606-8501, Japan; ⁱOkinawa Institute of Science and Technology, Graduate University, Okinawa 904-0412, Japan; ^jInstitució Catalana de Recerca i Estudis Avançats (ICREA), 08010 Barcelona, Spain

ABSTRACT Transmembrane adhesion receptors at the cell surface, such as CD44, are often equipped with modules to interact with the extracellular matrix (ECM) and the intracellular cytoskeletal machinery. CD44 has been recently shown to compartmentalize the membrane into domains by acting as membrane pickets, facilitating the function of signaling receptors. While spatial organization and diffusion studies of membrane proteins are usually conducted separately, here we combine observations of organization and diffusion by using high spatio-temporal resolution imaging on living cells to reveal a hierarchical organization of CD44. CD44 is present in a meso-scale meshwork pattern where it exhibits enhanced confinement and is enriched in nanoclusters of CD44 along its boundaries. This nanoclustering is orchestrated by the underlying cortical actin dynamics. Interaction with actin is mediated by specific segments of the intracellular domain. This influences the organization of the protein at the nano-scale, generating a selective requirement for formin over Arp2/3-based actin-nucleation machinery. The extracellular domain and its interaction with elements of ECM do not influence the meso-scale organization, but may serve to reposition the meshwork with respect to the ECM. Taken together, our results capture the hierarchical nature of CD44 organization at the cell surface, with active cytoskeleton-templated nanoclusters localized to a meso-scale meshwork pattern.

Monitoring Editor

Jennifer Lippincott-Schwartz
Howard Hughes Medical
Institute

Received: Nov 13, 2018

Revised: Aug 23, 2019

Accepted: Sep 27, 2019

This article was published online ahead of print in MBoC in Press (<http://www.molbiolcell.org/cgi/doi/10.1091/mbc.E18-11-0715>) on October 2, 2019.

[†]These authors contributed equally to the study.

*Address correspondence to: Satyajit Mayor (mayor@ncbs.res.in); Maria F. Garcia-Parajo (maria.garcia-parajo@icfo.eu).

Abbreviations used: BG, benzylguanidine; DBSCAN, density-based spatial clustering of applications with noise; DC-SPT, dual color single particle tracking; ECD, extracellular domain; ECM, extracellular matrix; FBS, fetal bovine serum; fps, frames per second; FR, folate receptor; FRET, Förster's resonance energy transfer; HA, hyaluronic acid; ICD, intracellular domain; Jas, Jasplankinolide; MEF, mouse

embryonic fibroblast; MSD, mean-squared displacement; PBS, phosphate-buffered saline; SPT, single particle tracking; STORM, stochastic optical reconstruction microscopy; TALL, temporary arrest of lateral diffusion; TIRF, total internal reflection fluorescence; Tm, transmembrane domain.

© 2020 Sil, Mateos, et al. This article is distributed by The American Society for Cell Biology under license from the author(s). Two months after publication it is available to the public under an Attribution–Noncommercial–Share Alike 3.0 Unported Creative Commons License (<http://creativecommons.org/licenses/by-nc-sa/3.0>).

"ASCB®," "The American Society for Cell Biology®," and "Molecular Biology of the Cell®" are registered trademarks of The American Society for Cell Biology.

INTRODUCTION

Heterogeneity in the distribution of membrane proteins and lipids is becoming an increasingly appreciated paradigm in the context of the organization of molecules at the plasma membrane (Sezgin *et al.*, 2017). This regulated, nonrandom distribution of membrane proteins, such as signaling receptors, is implicated in their molecular function and signaling output (Garcia-Parajo *et al.*, 2014). The advent of superresolution microscopy and breakthroughs in single molecule techniques has revolutionized our understanding of cellular organization at the molecular level (Kusumi *et al.*, 2005; Klotzsch and Schütz, 2013; van Zanten and Mayor, 2015). The major goal from such techniques has traditionally been to obtain detailed descriptions of protein clustering, cluster sizes, or intermolecular distances. However, these superresolution techniques are often technically demanding, and associated invasive sample preparation methods are fraught with criticism for being nonphysiological. Additionally, although such studies of membrane constituents inform us on the organizational details at the molecular level, there have been fewer efforts to understand the organization and dynamics of proteins at larger spatial scales, to ascertain whether there exists any spatial hierarchy in membrane protein organization.

Studies of the membrane organization of many transmembrane receptors such as TCRs, EGFR, E-cadherin, GPCRs, or chemokine receptors such as CXCR-4 have advanced our understanding of changes at the nano-scale due to receptor dimerization or oligomerization (~2–40 nm) in the presence or absence of the cognate ligand (Overton and Blumer, 2000; Terrillon and Bouvier, 2004; Hofman *et al.*, 2010; Beck-García *et al.*, 2015; Strale *et al.*, 2015; Pagon *et al.*, 2016; Martinez-Munoz *et al.*, 2018). At the same time, studies elucidating the inhomogeneous diffusion behavior of membrane proteins such as transferrin receptors (Kusumi and Sako, 1996) or CD44 (Freeman *et al.*, 2018) have revealed the presence of compartments in the cell membrane at a larger length scale (approximately a few hundred nanometers), templated by the underlying cytoskeletal meshwork. The potential hierarchy in the nature of organization of membrane proteins has been speculated in the past based on evidences from clustering and diffusion studies of different proteins (Kusumi *et al.*, 2011). It is likely that a unified study of diffusion and organization interrogating the distribution of a particular membrane protein at different spatial scales will provide information of any underlying hierarchy in spatial scales of organization.

Type-1 transmembrane proteins are a major and abundant class of integral membrane proteins that span three distinct environments: the extracellular space, transmembrane, and cytoplasmic milieu. The lymphocyte homing receptor CD44, is a type I transmembrane protein involved in cell-matrix adhesion (Ponta *et al.*, 2003). It has a heavily glycosylated extracellular domain (ECD) that ensures binding to extracellular lectins such as galectins, besides being able to bind to its ligand hyaluronic acid (HA) as well as other components of the extra cellular matrix such as fibronectin and osteopontin (Ponta *et al.*, 2003; Senbanjo and Chellaiah, 2017). Previous studies have shown that the ECD of CD44 is clustered by Galectin-3, which in turn also binds glycosphingolipids and is important for the endocytosis of the protein by a clathrin-independent pathway (Howes *et al.*, 2010; Lakshminarayan *et al.*, 2014). Additionally, HA binding has been shown to influence the dynamics of the protein at the plasma membrane (Lakshminarayan *et al.*, 2014; Freeman *et al.*, 2018). The juxtamembrane O-glycosylation site and the transmembrane region with two putative palmitoylation sites confer the ability on the protein to partition into detergent-resistant membrane fractions or cholesterol-enriched domains on the plasma membrane (Thankamony and Knudson, 2006; Shao *et al.*, 2015).

At the intracellular side, the relatively short 70 amino acid–long cytoplasmic tail of CD44 interacts with multiple cytoskeletal adaptor proteins. The association of the protein with ezrin has been shown to be important for T-cell migration in interstitial spaces of endothelial cells (Mrass *et al.*, 2008). The interaction with ezrin also influences the protein's ability to act as membrane picket in macrophages providing a functional partitioning of the FcγRIIA at the plasma membrane and facilitating its phagocytic function in macrophages (Freeman *et al.*, 2018). Ankyrin binding has been shown to be important for HA binding by CD44 (Bourguignon, 2008). A proteomic analysis of the interacting partners of the CD44 cytoplasmic tail has also revealed an interaction with other cytoskeletal adaptors such as vinnexin, IQGAP1 and talin1 (Skandalis *et al.*, 2010). The modularity of these potential cytoskeletal interactions in the tail of CD44 via its multiple cytoskeletal adaptor binding sites opens up possibilities to study how they may independently regulate organization and turnover of the protein at the cell surface.

Thus, the diverse structural attributes of CD44 impart this receptor with the ability to be influenced by extracellular interactions, membrane composition, and the actin cytoskeleton. Hence, it also provides an ideal platform to uncover general principles of how such molecules are organized at varying length scales, determined by distinct modes of interaction in the different milieu and also the interplay between these length scales. Nevertheless, studies so far have not systematically investigated the role of the different structural domains of the protein in the organization and dynamics of the liganded, as well as the native unliganded receptor on the membrane, at multiple spatial scales.

In this study, we have exploited various imaging methods in living cells to characterize the organization of CD44 at the single molecule level over multiple spatiotemporal scales. Single molecule tracking at different labeling densities allowed us to capture the dynamics of CD44, at both the nano- and meso-scale levels. We define nano-scale organization as being built of individual molecules brought together within an ~10-nm scale and meso-scale as domains ~100 nm–<1 μm in scale. By means of interleaved homo-Förster's resonance energy transfer (FRET)-based anisotropy and high-density single molecule imaging, we show that the meso-scale organization of CD44 is significantly associated with its nanoclusters. Moreover, homo-FRET anisotropy measurements revealed a role for the actomyosin machinery and formin, which is also reflected in the mesoscale organization. Overall, our data provide evidence for a hierarchical organization of CD44, wherein each layer of organization is determined by distinct interactions of the receptor.

RESULTS

Spatiotemporal mapping of CD44 reveals a meshlike distribution of the protein at the mesoscale

To explore the dynamics of CD44 with high spatiotemporal resolution, we utilized the standard isoform of mouse CD44 (Ponta *et al.*, 2003) tagged with a SNAP domain at the N-terminus and GFP at the C-terminus (SNAP-CD44-GFP) (Figure 1, a and b; Supplemental Table S1). This chimeric protein can be labeled at the extracellular side using cell-impermeable benzylguanine (BG)-conjugated fluorophores that covalently link to the extracellular SNAP domain. SNAP-CD44-GFP was expressed in wild-type mouse embryonic fibroblast (MEF) cells that endogenously express CD44 as well as produce the ligand HA (Gerecht *et al.*, 2007; Siiskonen *et al.*, 2015) and labeled with SNAP-Alexa 546 (or BG-Alexa 546). Subsaturation labeling conditions (≤30 nM) were required for performing single particle tracking (SPT) in order to unambiguously reconstruct all the individual receptor trajectories of diffusion. However, this approach

undersamples the cell membrane and thus provides little information on membrane regions dynamically explored by the receptor (Figure 1b). We thus increased the labeling density (~50–100 nM), to ensure higher sampling frequencies of the membrane protein and yet maintaining the ability of detecting individual molecules in each single frame to determine their coordinates with subpixel accuracy (Figure 1c).

Time-lapse images were acquired at 10 frames per second (fps) for 1000 s, and the spatial coordinates of identified individual molecules over multiple frames were collapsed into a single frame to obtain a time-dependent cartography of the regions dynamically explored by the receptor as described in an earlier study (Torrenopina *et al.*, 2014). This density regime offers the possibility of building up a large number of localizations to construct dynamic meso-scale cartography of CD44 distribution over the entire cell membrane (Figure 1c). Remarkably, we found that CD44 diffusion and distribution are largely inhomogeneous, describing a clear meshlike spatiotemporal distribution at the meso-scale (Figure 1c', zoomed in). This mesh is defined by regions frequently revisited by the receptor and/or induced by its temporal arrest on the cell membrane. This is in stark contrast with the distribution of simulated randomized localizations on the plasma membrane (Figure 1, d and d'), which appears homogeneous at the same length scale. Indeed, enlarged regions of the cartography, from the same patch of the cell membrane, generated at two different time windows, show the dynamic character of the mesh (Figure 1, e and e'), and importantly, reveal sites of confinement/trapping of the receptor, evidenced by the large number of localizations (>10⁶ for Figure 1c) occurring within regions between ~90 and 200 nm in size (Supplemental Figure S1b). Moreover, some of these regions have a long persistence time (~50–60 s, Figure 1, e and e', and merged image in e'), indicating that the receptors could be stably confined in these regions and/or transiently tether repeatedly to the same regions. Similar experiments conducted in cells that exhibit very low surface levels of endogenous CD44 (COS-7 cells; Supplemental Figure S1, a and a') and the extracellular ligand, HA (Knudson *et al.*, 1993; Shyjan *et al.*, 1996) (CHO cells in Supplemental Figure S1c), also yielded similar results. Together, these results indicate that CD44 is organized in a meshwork pattern on the plasma membrane and this distribution is independent of binding to its ligand HA on the extracellular side or surface levels of endogenous proteins.

Since the experiments were conducted on the surface of the cell close to the coverslip, it is conceivable that the observed meso-scale pattern visualized for CD44 could be an artifact of the patterning of the membrane due to its adhesion to the cell substrate. To rule this out, we imaged MEFs expressing SNAP-CD59-GPI, a GPI anchored protein, unrelated to CD44. Analysis of the meso-scale map of SNAP-CD59-GPI also reveals a meso-scale meshwork pattern on the cell surface, indicating a compartmentalized state of the plasma membrane (Supplemental Figure S1f). To additionally rule out the possibility that overexpression of the chimeric SNAP-tagged CD44 protein induces such a distribution, we investigated how endogenous CD44 is organized at the plasma membrane by labeling the protein using anti-CD44 antibody and performing stochastic optical reconstruction microscopy (STORM) in fixed CHO cells (Supplemental Figure S1d). Endogenous CD44 at nonadherent membrane of the lamella, away from the adhesion surface, also revealed a meshworklike pattern of the protein at the meso-scale. STORM revealed a nano-scale clustered distribution of CD44 laid out in a nonrandom mesoscale meshlike pattern at the cell membrane. Nearest neighbor distance analysis on CD44 clusters of multiple

STORM images further confirmed that the nanoclusters of CD44 are distributed in a manner distinct from simulated randomized distribution of nanoclusters (Supplemental Figure S1e). Therefore the meshworklike pattern of CD44 reflects a hitherto unappreciated intrinsic organization of this protein in the membrane of living cells.

To discriminate between single and/or multiple receptors being confined, as obtained in the cartography, we then turned to dual color SPT (DC-SPT) by using subsaturation labeling conditions (Kusumi *et al.*, 2005). For this, we labeled the SNAP-CD44-GFP expressed in MEFs using two different dyes (JF549-cpSNAP and JF646-SNAP ligands) and tracked the motion of the receptor at 60 fps for 400 frames (6.7 s) (Supplemental Videos S1 and S2). Localization maps created from superposing 400 frames of the DC-SPT images revealed typical trajectories of Brownian diffusion interspersed with transiently confined trajectories of the single color tracks (Supplemental Figure S2a). Analysis of >2500 trajectories reveals the existence of a large percentage of transiently confined receptor (68.4 ± 2.3%) on the cell membrane with majority of confinement time restricted to ≤ ~3s (Table 1 and Supplemental Figure S2b). When we examined the DC-SPT data, we observed a noticeable overlap of CD44 molecules (colocalized) that reside in confined regions (Figure 1f; purple arrowheads indicate black dots in the map and corresponding trajectories). To quantify specific colocalization, we determined the occurrence of colocalized events as a function of interparticle distances within defined areas (depicted as radius on the x-axis in Supplemental Figure S2c) and compared the results to those of diffusion from randomized trajectories (obtained from 180° flipped images of the same regions). A random distribution is expected to have an interparticle distance distribution index equal to 1, with values greater and smaller indicating clustering and dispersion, respectively (Clark and Evans, 1954). From the interparticle distance quantification, we defined colocalized particles as those that exhibited interparticle distances (between two differently labeled SNAP-CD44-GFP molecules) less than 200 nm for three consecutive frames. We also observe a subset of these events to correspond to interparticle distance <100 nm (a length scale more precisely matched with combined localization precision of the fluorophores) (Figure 1f). Interestingly, the length scale over which CD44 exhibits colocalization corresponds to the length scale over which it exhibits transient confinement as is evident from analyzing the step size distribution (Figure 1g). We also quantified the colocalization lifetime and find that individual colocalization event lasts for <100 ms (Figure 1h). Temporal analysis of localization events revealed recurrence of colocalization events at the same spatial coordinates over a period of 400 frames (0–6.7 s) (Figure 1i, color indicating time at which colocalization occurred), indicating hotspots of trapping of same/different pairs of receptors. These data thus indicate the existence of hotspots on the plasma membrane that can both restrict the diffusion of CD44 and recruit multiple CD44 molecules. Moreover, the cartography analysis, STORM, and DC-SPT data (Supplemental Figure S1, d and e; Figure 1f) suggest the formation of CD44 clusters that might be organized in a meso-scale meshwork on the plasma membrane.

The dynamic meso-scale meshwork of CD44 associates with its nanoclusters

STORM imaging of endogenous CD44 in CHO cells as described above, as well as an earlier study (Lakshminarayan *et al.*, 2014), provide evidence for the existence of nano-scale clusters of CD44 at the plasma membrane. Moreover, CD44 exhibits a high incidence of colocalizations (<200 nm) in DC-SPT as well as spatially confined

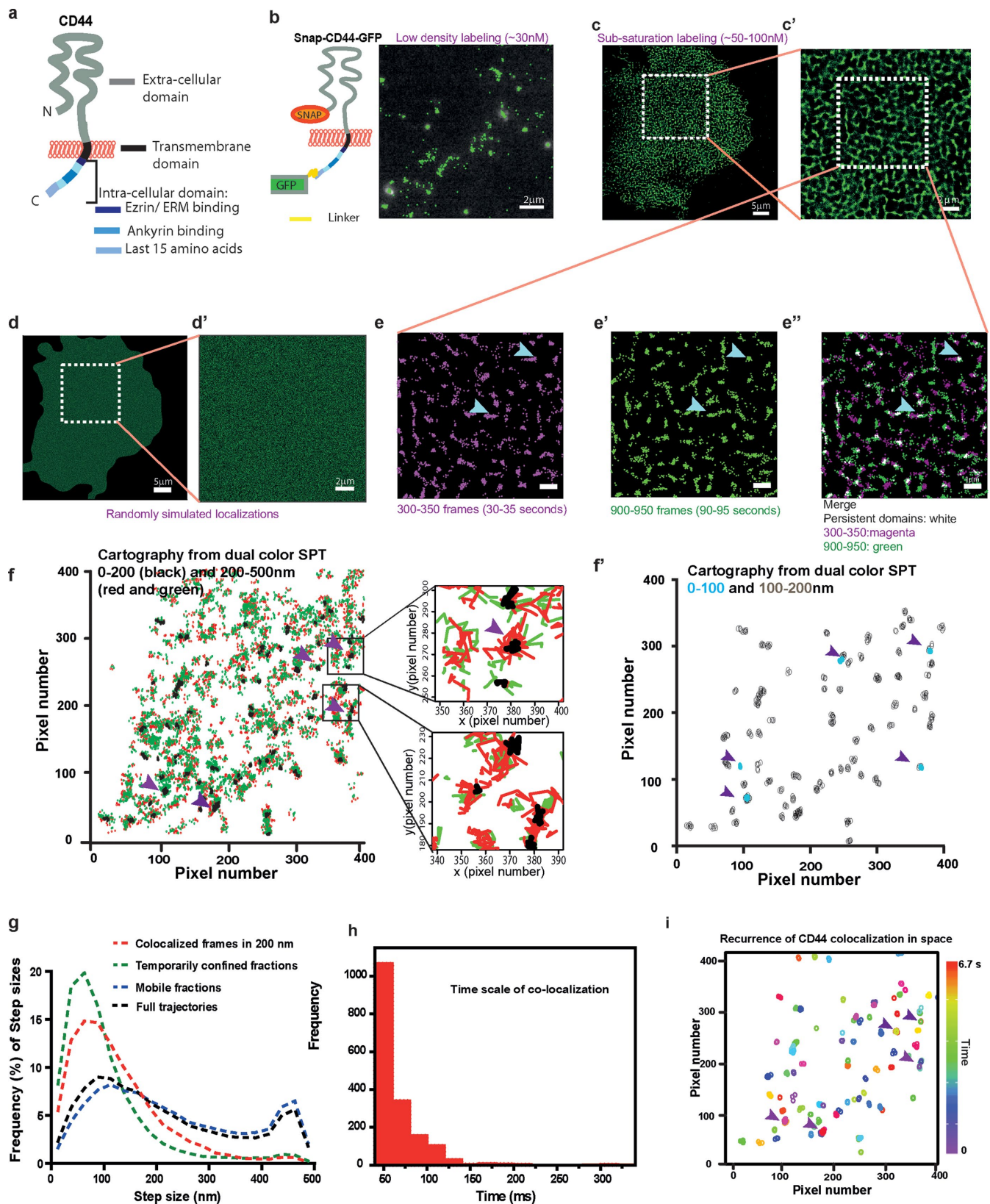


FIGURE 1: CD44 exhibits a nonrandom distribution at the plasma membrane at multiple spatiotemporal scales. (a) Schematic of a standard isoform of CD44 showing key domains of the protein, namely, the ECD, the Tm, and the ICD. (b) Schematic of SNAP-CD44-GFP and representative dynamic cartography of CD44 obtained at sublabeled conditions (~30 nM). Each dot corresponds to the (x, y) coordinates (with subpixel accuracy) of individual receptors as they diffuse on the cell membrane. The (x, y) coordinates over 50 sequential frames are collapsed and overlaid into a single fluorescence frame. (c) Cartography of SNAP-CD44-GFP obtained at higher labeling conditions (~50–100 nM); (x, y) coordinates from 1000 frames (1,354,066 localizations) collapsed in a single map with a zoomed-in

Protein chimera	Percentage transient confinement	Trap radius (nm)	Diffusion coefficient ($\mu\text{m}^2/\text{s}$)
SNAP-CD44-GFP	68.4 ± 2.3	42.5 ± 1.6	0.02 ± 0.01 (slow: $\sim[69 \pm 4]\%$) 0.16 ± 0.01 (fast: $\sim[31 \pm 10]\%$)
SNAP-CD44TmICD-GFP	57.1 ± 4.2	54.9 ± 4.6	0.02 ± 0.01 (slow: $[49.3 \pm 3.2]\%$) 0.18 ± 0.004 (fast: $[50.7 \pm 9.9]\%$)
SNAP-CD44Tm-GFP	45.4 ± 8.3	68.9 ± 11.7	0.06 ± 0.02 (slow: $[29.5 \pm 9.5]\%$) 0.23 ± 0.01 (fast: $[70.5 \pm 4.4]\%$)

TABLE 1: CD44 diffusion characteristics from SPT.

localizations that emerge as a meshlike pattern in the cartography analysis. Together, these observations motivated us to investigate the clustering interactions of CD44 at the nano-scale using homo-FRET microscopy (Ghosh *et al.*, 2012).

Fluorescence emission anisotropy-based homo-FRET measurements probes the proximity of fluorescently tagged proteins at a molecular length scale \sim Forster's radius (~ 5 nm for the GFP fluorophore; Ghosh *et al.*, 2012) on the living cell membrane, reporting molecular interactions at a length scale ~ 10 times smaller than achievable resolution in STORM. Using this method, we identified regions of low and high anisotropy in the membrane of unperturbed living cells in four different cell types: COS-7 cells (Figure 2a; Supplemental Figure S3, d and d'), CHO cells (Figure 3, b and d), MEFs (Supplemental Figure S3, f and f'), and MCF-7 (Supplemental Figure S3, e and e'), each of which has different properties. While CHO and MEFs express endogenous CD44, COS-7 and MCF-7 cells have very low surface levels of endogenous protein (Supplemental Figure S3g), and both COS-7 and CHO cells do not synthesize a major extracellular matrix (ECM) component, HA, that can bind CD44 from the extracellular side (Shyjan *et al.*, 1996; Yang *et al.*, 2012). The regions of low anisotropy correspond to an enrichment of CD44-GFP molecules at ≤ 5 nm intermolecular distances, thus indicating the occurrence of nanometer scale encounters of CD44 molecules on the cell membrane at a steady state. These results corroborate the colocalization observed by DC-SPT as well as spatially confined localizations observed in the cartography.

To ascertain the relationship between nano- and meso-scale dynamic organization of CD44, we expressed the SNAP-CD44-GFP construct in COS-7 cells to obtain fluorescence emission anisotropy maps from the GFP tag on the SNAP-CD44-GFP, interleaved with single molecule imaging data from the subsaturation labeled SNAP tag, amenable for generating cartography. We

chose COS-7 cells since they exhibit low levels of CD44 at the cell surface and also on ensuring that these cells exhibit nanoclustering of ectopically expressed CD44-GFP (Supplemental Figure S3, d, d', and g) (Jiang *et al.*, 2002; Yang *et al.*, 2012). We selected different anisotropy ROIs and superimposed the corresponding spatial coordinates of individual molecules integrated over 40 frames (20 frames preceding and 20 frames following the anisotropy image) (Figure 2, b and c). We restricted our analysis to windows of 40 frames around an anisotropy image to reduce temporal variations that might occur between the anisotropy and cartography (see *Experimental Methods*). We then identified spatially restricted enriched localizations, termed localization hotspots on the cartography maps and classified these localization hotspots according to the corresponding anisotropy value (see *Experimental Methods* and Figure 2, c, c', c'', and d). A significantly higher fraction of localization hotspots were localized to regions of low anisotropy and correspondingly such localization hotspots were consistently depleted from the high anisotropy regions when compared with randomly dispersed localizations (Figure 2e). These data indicate that the meso-scale regions observed on the cartography overlaps with the regions of increased nano-scale clustering of the receptor. As a whole, our results reveal a multiscale organization of CD44 on the cell membrane with the distribution of nano-scale clusters correlated to the meso-scale meshwork. This motivated an exploration of the mechanism behind the formation of the nanoclusters of CD44.

The extracellular domain (ECD) and intracellular domain (ICD) of CD44 independently affect nanoclustering of CD44 at the plasma membrane

To probe the mechanism(s) responsible for the organization of CD44 molecules at nano-scale proximity, we examined both

ROI (c). (d) Simulated cartography with similar number of localizations as in c, distributed in a random manner, and enlarged ROI. (e) Cartography construction of (x, y) coordinates in the marked ROI in c from 50 consecutive frames obtained at two different experimental time windows, between 30–35 s (magenta, e) and 90–95 s (green, e') and merged image (right, e''). Blue arrowheads highlight regions of confinement, and white dots represent persistent confinement regions or sites revisited by the receptor. (f) Cartography obtained from 400 frames (~ 6.7 s) of DC-SPT data obtained by colabeling CD44 with JF549-cpSNAP ligand and JF646 SNAP ligand. Green and red dots correspond to localizations with the two different dyes indicating interparticle distances between 200 and 500 nm and black dots correspond to interparticle distances < 200 nm. Zoomed-in ROIs depict the indicated reconstructed trajectories; f' shows the subset corresponding to localization of particles with 0–200 nm interparticle distance (black in f) where the interparticle distance corresponds to < 100 nm (blue circles) and 100–200 nm (gray circles). Note the < 100 nm colocalization events always correspond to regions where localizations at the larger length scale of 100–200 and 200–500 nm interparticle distance are also found (indicated by purple arrowheads in f and f'). (g) Frequency distribution of step sizes of particles from trajectories wherein particles exhibit colocalization (red), temporary arrest (green), mobile (blue), and from the full trajectories (black) (27,856 trajectories). (h) Frequency distribution of duration of colocalization of particles identified in f. Note the lifetime of colocalization is in the range of < 100 ms. (i) The 2D plot of all colocalized particles (< 200 nm) obtained from the trajectories identified in f, where purple arrowheads indicate colocalization events that occur repeatedly at the same spot over the time period of observation. Color LUT bar indicates observation time from 0 to 6.7 s.

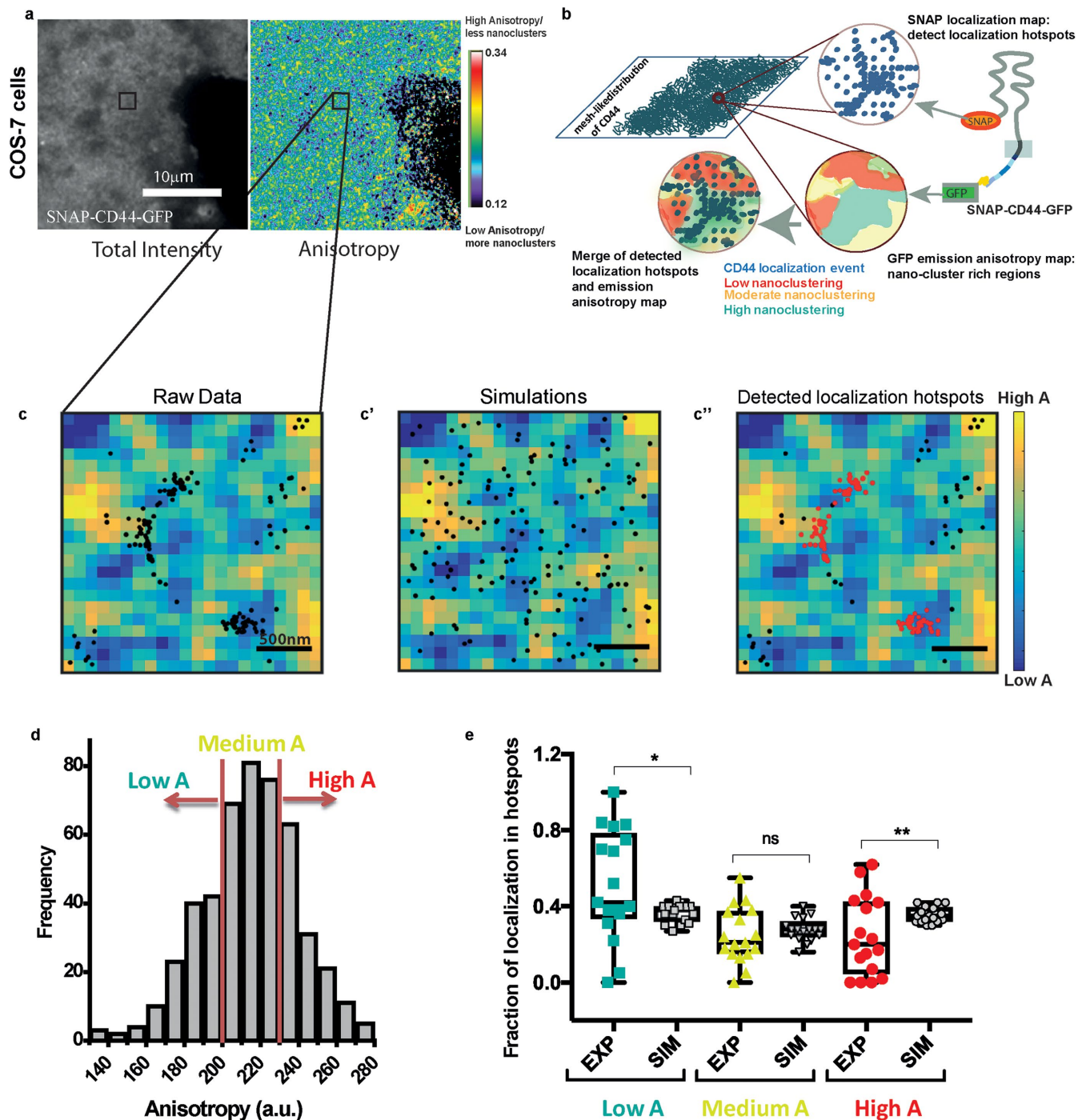


FIGURE 2: Meso-scale meshwork of CD44 colocalizes with regions enriched in CD44 nanoclusters. (a) Total GFP fluorescence intensity and anisotropy map of the SNAP-CD44-GFP protein expressed in COS-7 cells that exhibit low levels of surface CD44. Note that the anisotropy image shows regions of low anisotropy (blue) and high anisotropy (red), corresponding respectively, to regions enriched in or depleted of CD44 molecules in nano-scale proximity (CD44 nanoclusters). (b) Schematic depicting the methodology by which FRET based anisotropy maps was correlated to localization maps obtained from high-density single molecule imaging and cartography analysis. (c, c', c'') Representative ROI image depicting the anisotropy map overlaid with localizations from raw cartography images integrated over 40 frames (left), random localizations obtained from simulations (center), and detected localization hotspots (red dots) of SNAP-CD44-GFP (right). (d) Histogram of the anisotropy values for the ROI shown in c. Red vertical lines indicate the thresholds chosen to classify regions of low anisotropy (Low A), medium anisotropy (Medium A), and high anisotropy (High A), where medium anisotropy is binned around the median value of anisotropy in a given ROI. (e) Fraction of detected localizations in the localization hotspots in low, medium, and high anisotropy regions compared with simulated localizations. Each symbol in the plot corresponds to a single ROI, and the data are obtained from at least six different cells from > 15 ROIs. Difference between distributions has been tested using Kolmogorov-Smirnov test.

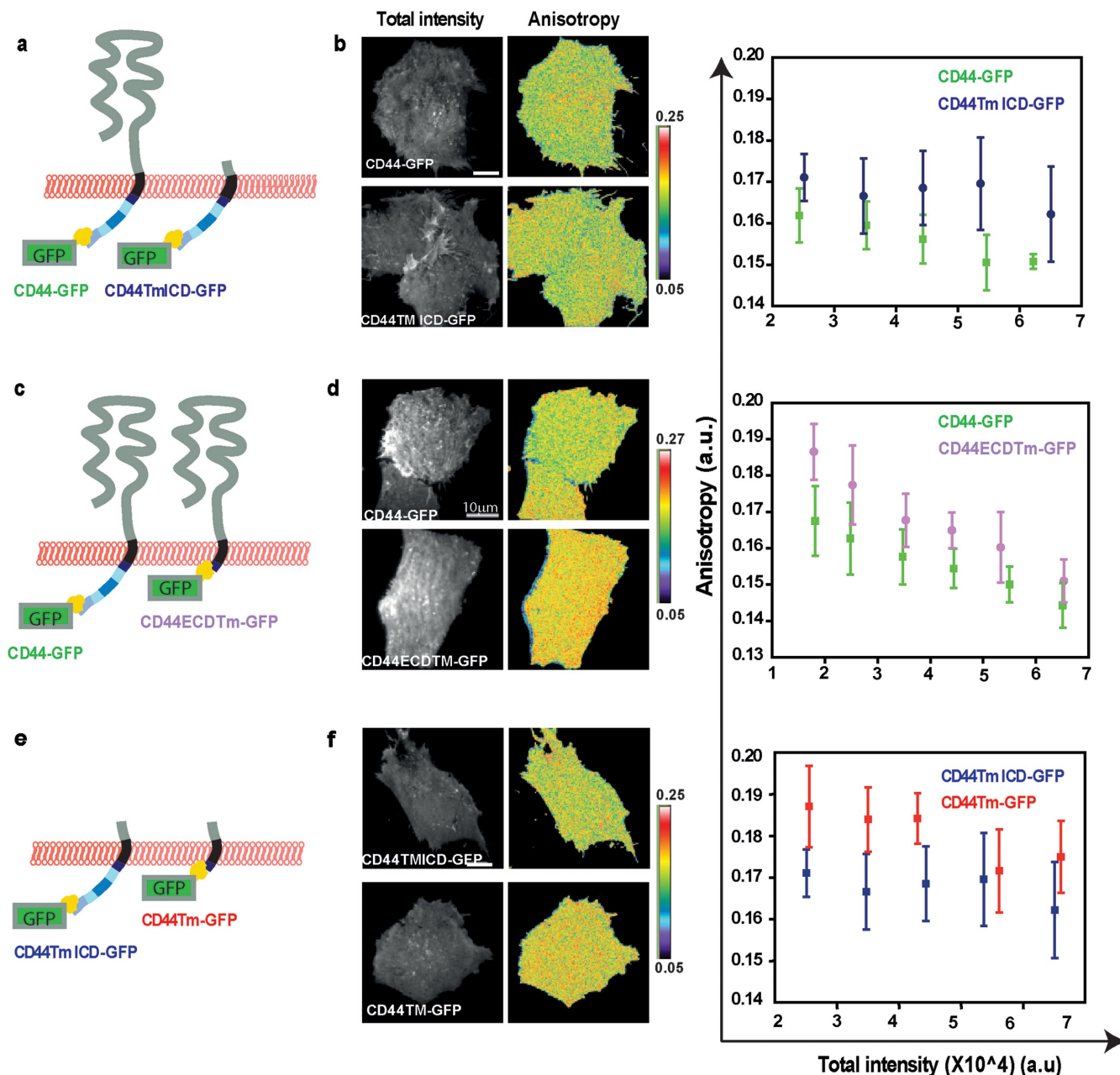


FIGURE 3: ECD and ICD independently affect CD44 nanoclustering. Schematics (a, c, and e) depict CD44-GFP constructs expressed in CHO cells used to generate the corresponding intensity and anisotropy images in b, d, and f. Anisotropy vs. intensity plots show a significant increase in anisotropy in the truncated protein lacking the ECD (a, b; $p < 10^{-43}$), ICD (c, d; $p < 10^{-58}$), or when the construct lacking the ECD (data from the same experiment as a and b) is compared with one lacking both ECD and the ICD (e, f; $p < 10^{-77}$). All raw distributions are statistically significant by Mann-Whitney test for each condition. (The data are from one representative experiment. [b] CD44-GFP = 20 fields, CD44TmICD-GFP = 27 fields. [d] CD44-GFP = 25 fields, CD44ECDTm-GFP = 13 fields. [f] CD44Tm-GFP = 15 fields.)

intensity dependence and spatial anisotropy distribution of various mutants of CD44-GFP (Figure 3, a, c, and e; Supplemental Table S1 for the description of the different constructs used) expressed in HA-deficient CHO cells by fluorescence emission anisotropy based homo-FRET microscopy. Fluorescence emission anisotropy of CD44-GFP was intensity dependent indicating a concentration-dependent change potentially due to 1) protein-protein interactions, 2) potential dilution by endogenous CD44, and 3) a combination of both (Figure 3b). The latter possibility was confirmed by using MCF-7 cells that have very low levels of cell

surface CD44, where fluorescence emission anisotropy of CD44GFP exhibited visibly lower intensity dependence, while at the high-intensity range, it became concentration dependent (Supplemental Figure S3, e and e). These observations suggest that at the lower expression range of CD44-GFP in cells with significant endogenous CD44, the intensity dependence of its anisotropy is a convolution of both, dilution by endogenous unlabeled protein as well as concentration-dependent protein-protein interactions. However, at higher levels of expression, protein-protein interactions and trivial density-dependent FRET may contribute to

the intensity dependence of anisotropy. Consistent with this, deletion of the ECD of CD44 (CD44TmICD-GFP) resulted in an increase in anisotropy and reduced its intensity dependence (Figure 3, a and b), consistent with an attenuation of concentration-dependent interactions as compared with the full-length receptor in CHO cells. While these cells do not synthesize HA (Shyjan *et al.*, 1996), CD44 expressed on the surface of these cells can still bind galectins (Lakshminarayan *et al.*, 2014) and may have other protein–protein interactions mediated by the ECD of the receptor. These interactions could lead to a concentration-dependent clustering, which is reduced by deletion of the ECD. Thus, the prominent intensity dependence and lower fluorescence emission anisotropy exhibited by the full-length receptor as compared with the mutant likely result from ECD interactions of CD44, impacting its nano-scale organization.

To ascertain whether the deletion of the ECD completely abolished CD44 nanoclustering, we measured the change in anisotropy of the fluorescently labeled CD44TmICD protein on dilution of fluorophores by photobleaching. Since enhanced GFP is capable of reversible photobleaching, giving rise to artifacts in bleaching-based homo-FRET measurement (Sinnecker *et al.*, 2005), we resorted to a different strategy for labeling the truncated CD44 with a fluorophore that exhibits reduction in energy transfer efficiency on destruction of FRET competent fluorophores by bleaching (Sharma *et al.*, 2004). We designed a chimeric folate receptor (FR)-tagged version of the ECD truncated protein (Supplemental Figure S3a). This chimeric construct was expressed in CHO cells and labeled with a fluorescently labeled folate analogue (PLB^{TMR}: N^α-pteroyl-N-Bodipy^{TMR}-L-lysine) (Goswami *et al.*, 2008) and then imaged while photobleaching the labeled cells. If the labeled proteins are clustered, the emission anisotropy of FR-CD44TmICD should increase since photobleaching reduces the concentration of fluorescent proteins engaged in energy transfer (Sharma *et al.*, 2004). PLB^{TMR}-labeled FR-CD44TmICD exhibited an increase in emission anisotropy on photobleaching (Supplemental Figure S3, b and c), indicating that the ECD truncated protein retains the ability to engage in nanometer scale homomeric interactions at the plasma membrane. The slope in the anisotropy plot is an indication of the extent of nanoclustering, that is, the higher the slope, the greater the extent of nanoclustering (Sharma *et al.*, 2004). Overall, these results indicate an inherent ability of CD44TmICD to nanocluster on the cell membrane, and the extent of clustering in CD44 is also modulated by interactions in the extracellular milieu.

The findings described above led us to investigate the role of the ICD in CD44 nanoclustering. For this, we measured the fluorescence emission anisotropy of the full-length receptor (CD44-GFP) and a CD44 mutant lacking only the ICD or cytoplasmic tail (CD44ECDTm-GFP) (Figure 3c). The results indicated that the full-length wild-type protein is clustered to a greater extent compared with the ICD truncated protein, as indicated by the lower anisotropy values obtained with the full-length protein (Figure 3d). The truncated protein still retains a concentration-dependent anisotropy, consistent with the possibility of passive interactions affecting its nanoclustering. A similar increase in anisotropy values was obtained in COS-7 and MCF-7 cells transfected with the same constructs (Supplemental Figure S3, e and e'), indicating that the results obtained in the CHO cells (Supplemental Figure S3, d and d') were minimally affected by the endogenous, unlabeled CD44 population at the cell surface. Consistent results were also obtained in MEF cells that secrete HA and express significant levels of endogenous CD44, indicating that the disruption of nanoclustering due to the loss of the ICD in these cells is strong enough to manifest as a significant

increase in anisotropy, in spite of the presence of the polymeric ligand HA in the extracellular milieu as well as potential fluorophore dilution due to coclustering of labeled CD44 with endogenous unlabeled CD44 proteins (Supplemental Figure S3, f and f').

To further validate the clustering potential of the cytoplasmic domain, we deleted the entire ICD in the CD44TmICD-GFP construct to create a transmembrane domain (Tm)-only protein (CD44Tm-GFP) (Figure 3e). We found that the anisotropy of the resultant protein increased compared with the CD44TmICD-GFP (Figure 3f), consistent with the clustering potential of the ICD. Differences in nanoclustering in the presence and absence of the ICD were further corroborated by comparative photobleaching analysis of FR-tagged FR-CD44TmICD and the truncated FR-CD44Tm in CHO cells. We found that FR-CD44TmICD is clustered to a greater extent than FR-CD44Tm (Supplemental Figure S3, a–c), as indicated by a reduction in the slope of the anisotropy vs. normalized intensity curve of the transmembrane FR-CD44Tm as compared with the FR-CD44TmICD protein.

The results show that ECD and ICD independently affect CD44 nanoclustering. The ECD has a greater impact in establishing passive interactions with partners on the cell membrane giving rise to a strong intensity/expression level dependent clustering of CD44 at the cell surface. Even though the transmembrane region appears to have small but detectable ability to nanocluster the receptor (due to a minor residual slope in the photobleaching analysis), it is the ICD that strongly enhances the nanoclustering ability of CD44.

CD44 nanoclustering correlates with its tethering strength on the plasma membrane

To further understand how CD44 nanoclustering affects the lateral diffusion of the receptor, we carried out SPT at subsaturation labeling conditions (~30 nM) on the full-length SNAP-CD44-GFP (Supplemental Videos S3 and S4) and the truncated SNAP-CD44TmICD-GFP (Supplemental Video S5) and SNAP-CD44Tm-GFP (Supplemental Video 6) constructs in MEFs cells (Figure 4a). These cells are also ideally suited for testing the effect of the extracellular influence of HA, which may affect CD44 dynamics at the membrane. Individual trajectories for the three different constructs were obtained (Figure 4b; Supplemental Figure S4a), and the fractions of mobile trajectories were quantified (Figure 4c; calculated from escape probability of molecules in MEFs; Supplemental Figure S4, c and d are in COS-7 cells; Table 1); trajectories with diffusion coefficients <0.02 $\mu\text{m}^2/\text{s}$ were defined as immobile. Deletion of the ECD increased the fraction of mobile receptors as compared with the full-length protein (Figure 4c), an effect that became even more pronounced with further removal of the ICD. Moreover, analysis of the transient confinement areas showed tighter regions of confinement for the SNAP-CD44-GFP and SNAP-CD44TmICD-GFP as compared with the SNAP-CD44Tm-GFP mutant (Figure 4d, Supplemental Figure S4e, and Table 1), and the overall diffusion coefficients were significantly slower for the full-length receptor (Figure 4e; Table 1). The results indicate that interactions by the ECD ensure slower diffusion and the cytoplasmic domain ensures both slower diffusion and tighter confinement of CD44 at the plasma membrane. The difference between the wild-type protein and mutant-lacking ECD is more pronounced in MEFs compared with COS-7 cells, potentially owing to the presence of HA in the matrix of MEFs, consistent with the observations made in the earlier study by Freeman *et al.* (2018).

To further elucidate the consequences of the differences in tethering strength of the wild type and the transmembrane mutant as observed in the single color SPT experiments, analysis of colocalization

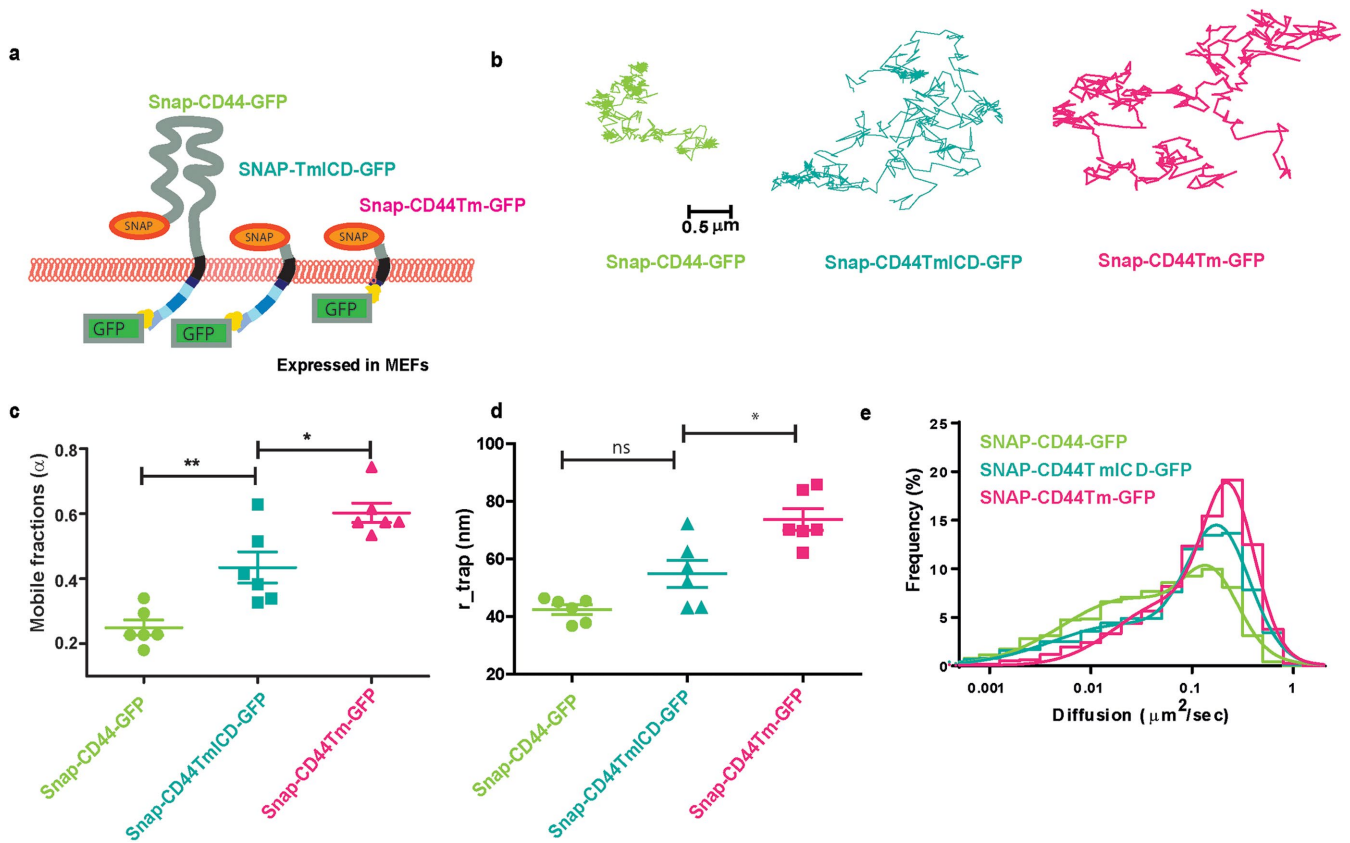


FIGURE 4: Extent of CD44 nanoclustering correlates with the strength of tethering on the cell membrane. (a) Schematic show SNAP-tagged constructs expressed in MEFs, utilized for SPT. (b) Representative trajectories for the indicated constructs show distinct diffusion characteristics of the different constructs. (c–e) Quantification of the (c) mobile fraction by escape probability method, (d) confinement radius (r_{trap}), (e) and diffusion coefficients of the full length and the truncated mutants. The data are derived from at least six cells for each construct. Number of trajectories: SNAP-CD44-GFP = 2977; SNAP-CD44TmICD-GFP = 2783; SNAP-CD44Tm-GFP = 4744.

events and quantification of interparticle distance using DC-SPT on both the full-length receptor and the transmembrane mutant lacking both the ECD and ICD further corroborated that interactions by these domains can affect the colocalization propensity of the protein (Supplemental Figure S2, e, e', f, and f'). Together with the anisotropy data (Figure 3; Supplemental Figure S3) these results point to a strong correlation between the degree of CD44 nanoclustering and its tethering at the cell membrane: the full-length receptor exhibits the strongest nanoclustering (as derived from the fluorescence anisotropy analysis) and tighter confinement and/or tethering at the cell membrane. On the other hand, deletion of both the ECD and cytoplasmic tail reduces nanoclustering and increases the mobility of the receptor, with reduced tethering at the membrane (Table 1).

Meso-scale organization of CD44 is influenced by its cytoplasmic interactions

Since CD44 nanoclustering is spatially correlated to its meso-scale distribution, we then tested whether alteration in the nanoclustering potential of the different mutants correlates with the manifestation of any defects in their meso-scale organization. SNAP-CD44-GFP, SNAP-CD44TmICD-GFP, and SNAP-CD44Tm-GFP constructs were expressed in MEFs, exogenously labeled, and imaged at a temporal resolution of 10 fps, as described earlier, in order to generate cartography of the different constructs (Figure 5a). Visual inspection of the cartography already shows more tightly bound localizations in the case of the full-length receptor and a larger number of dis-

persed localizations for the SNAP-CD44Tm-GFP mutant. Comparison of the confinement areas revealed similar confinement strength for the full-length receptor ($0.028 \pm 0.013 \mu\text{m}^2$) and the mutant lacking the ECD ($0.027 \pm 0.013 \mu\text{m}^2$) (Figure 5, b and c), indicating that the ECD does not play a major role on the meso-scale organization of the receptor. Consistent with these results, we did not find significant differences on the fractional number of localizations found on the meshwork between the full-length receptor (SNAP-CD44-GFP) and the mutant lacking the ECD (SNAP-CD44TmICD-GFP) (Figure 5d). In contrast, the mutant lacking the cytoplasmic tail as well as the ECD (SNAP-CD44Tm-GFP) exhibited larger confinement areas ($0.032 \pm 0.013 \mu\text{m}^2$) (Figure 5, b and c) and a significantly lower number of localizations associated to the meshwork as compared with the full-length receptor (SNAP-CD44-GFP) or the mutant lacking the ECD alone (SNAP-CD44TmICD-GFP) (Figure 5d). This result strengthens the observation from SPT that the cytoplasmic domain mediates tight confinement of the receptor at the plasma membrane.

We also performed similar experiments in HA-deficient COS-7 cells and obtained comparable results (Supplemental Figure S5). Since the confinement areas and number of localizations associated to the meshwork result from multiple revisiting and/or arrest of the receptor to the underlying meshwork, these results strongly suggest that the mutant lacking both the ECD and the cytoplasmic tail (SNAP-CD44Tm-GFP) compared with the mutant lacking the ECD alone (SNAP-CD44TmICD-GFP) is less tethered to the meshwork.

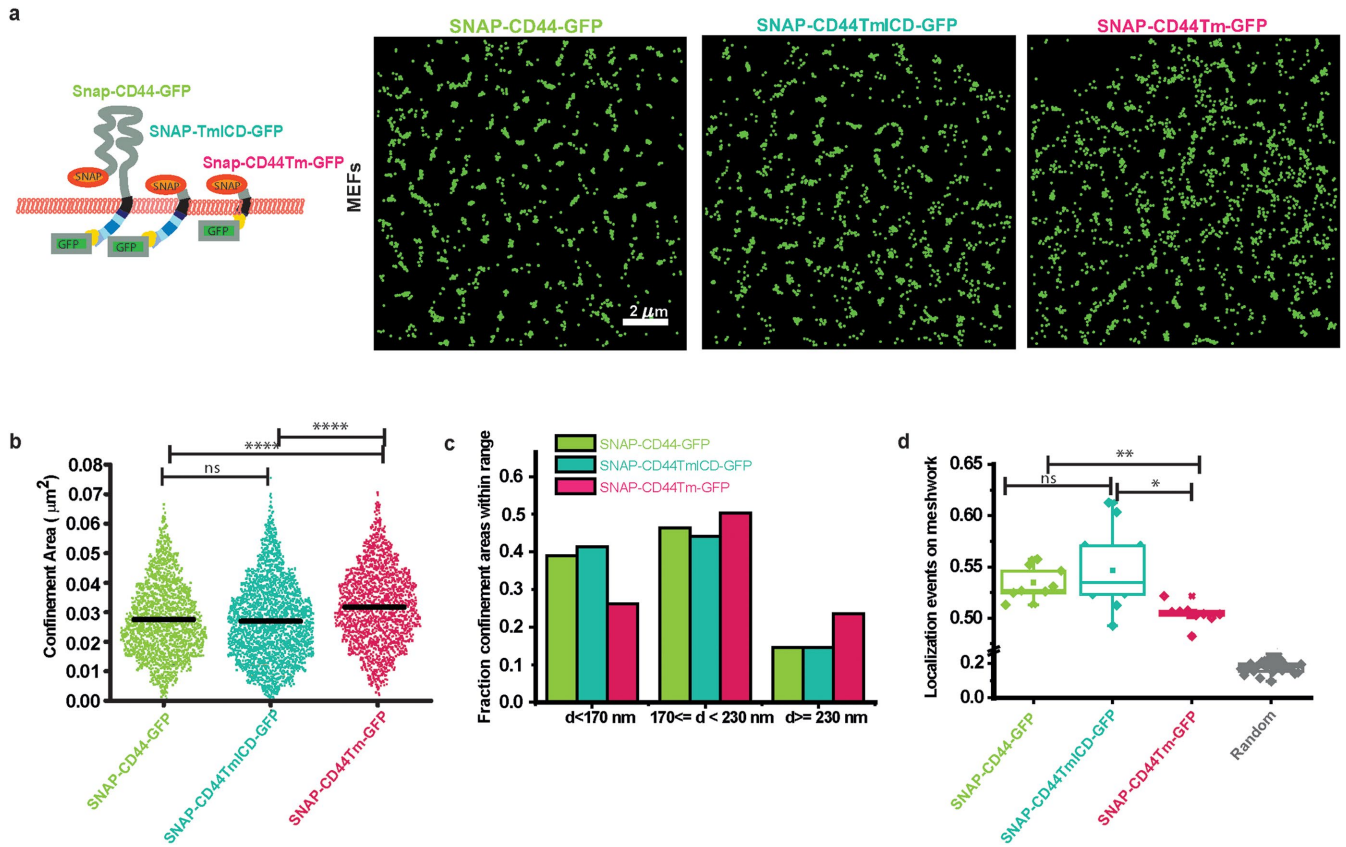


FIGURE 5: Meso-scale organization of CD44 is determined primarily by interactions of the ICD. (a) Representative cartography maps of the indicated CD44 constructs expressed in MEFs obtained from imaging at 10 fps and accumulating the spatial coordinates of individual molecules over 2 s (20 frames). (b) Quantification of the confinement areas for the different constructs during 2 s. Black lines correspond to the mean value. (c) Relative fractions of confinement areas for the different constructs, classified as a function of the confinement length, i.e., $d < 170 \text{ nm}$, $170 < d < 230 \text{ nm}$, or $d \geq 230 \text{ nm}$. (d) Fraction of localization events that belong to the meshwork for the different constructs and compared with the fraction of similar type of localizations measured from randomized localizations. The data are from one representative experiment. The experiment has been conducted at least twice with similar results. Data were obtained from a number of cells expressing SNAP-CD44-GFP (8), SNAP-CD44TmICD-GFP (11), or SNAP-CD44Tm-GFP (9). Difference between distributions was tested for significance using Kruskal–Wallis and post hoc test with Tukey–Kramer. (b) SNAP-CD44-GFP and SNAP-CD44TmICD-GFP: $p = 0.258 \rightarrow \text{ns}$; SNAP-CD44-GFP and SNAP-CD44Tm-GFP: $p < e^{-9}$; SNAP-CD44TmICD-GFP and SNAP-CD44Tm-GFP: $p < e^{-9}$. (d) SNAP-CD44-GFP and SNAP-CD44TmICD-GFP: $p = 0.8564 \rightarrow \text{ns}$; SNAP-CD44-GFP and SNAP-CD44Tm-GFP: $p < 0.005$; SNAP-CD44TmICD-GFP and SNAP-CD44Tm-GFP: $p = 0.0218$. SNAP-CD44Tm-GFP ($n = 9$ cells), SNAP-CD44TmICD-GFP ($n = 11$ cells), SNAP-CD44-GFP ($n = 8$ cells).

Of note, we also performed simulations of random localizations and overlaid them to an experimentally obtained meshwork to obtain a “basal” fraction of localizations that are stochastically found over the meshwork (labeled as random in Figure 5d). Comparison with the *in silico*–generated data revealed that even in the absence of the cytoplasmic tail, the SNAP-CD44Tm-GFP mobility is somewhat constrained by this underlying mesh albeit to a lower extent than the cytoplasmic domain containing counterparts. Therefore, our results strengthen the arguments for cytoplasmic interactions as a major player in orchestrating the nano- and meso-scale organization of CD44. Since the cytoplasmic tail of CD44 interacts with multiple cytoskeletal adaptor proteins such as ezrin and ankyrin (Bourguignon, 2008; Mrass *et al.*, 2008), our results suggest that CD44 nano-clustering might be induced by its tethering to the actin cytoskeleton. This finding resonates with the recently published results of CD44 in macrophages where diffusion characteristics of the protein are affected by tethering to the cytoskeleton mediated by ezrin (Freeman *et al.*, 2018) and leads us to investigate the role of the

actin cytoskeleton in the nanoclustering as well as the meso-scale organization of the protein.

Nanoclustering of CD44 is regulated by actin dynamics

Previous work has shown that actin binding confers the ability of proteins to associate with the actomyosin-clustering machinery in living cells. Here, dynamic actin filaments driven by myosin propel the formation of actin asters, driving the generation of clusters of proteins that associate with these structures (Gowrishankar *et al.*, 2012). Since CD44 has been shown to engage with the cytoskeleton by binding to ezrin and ankyrin via its cytoplasmic tail (Bourguignon, 2008; Mori *et al.*, 2008; Donatello *et al.*, 2012), we investigated whether actomyosin perturbations would affect the clustering of the receptor. Here we investigated the effects of actomyosin perturbations in CHO cells, since the ICD of CD44 was found to support nanoclustering of CD44 in all the cell types tested. First, we treated CHO cells with the actin filament stabilizer Jasplakinolide (Jas) to create blebs that represent

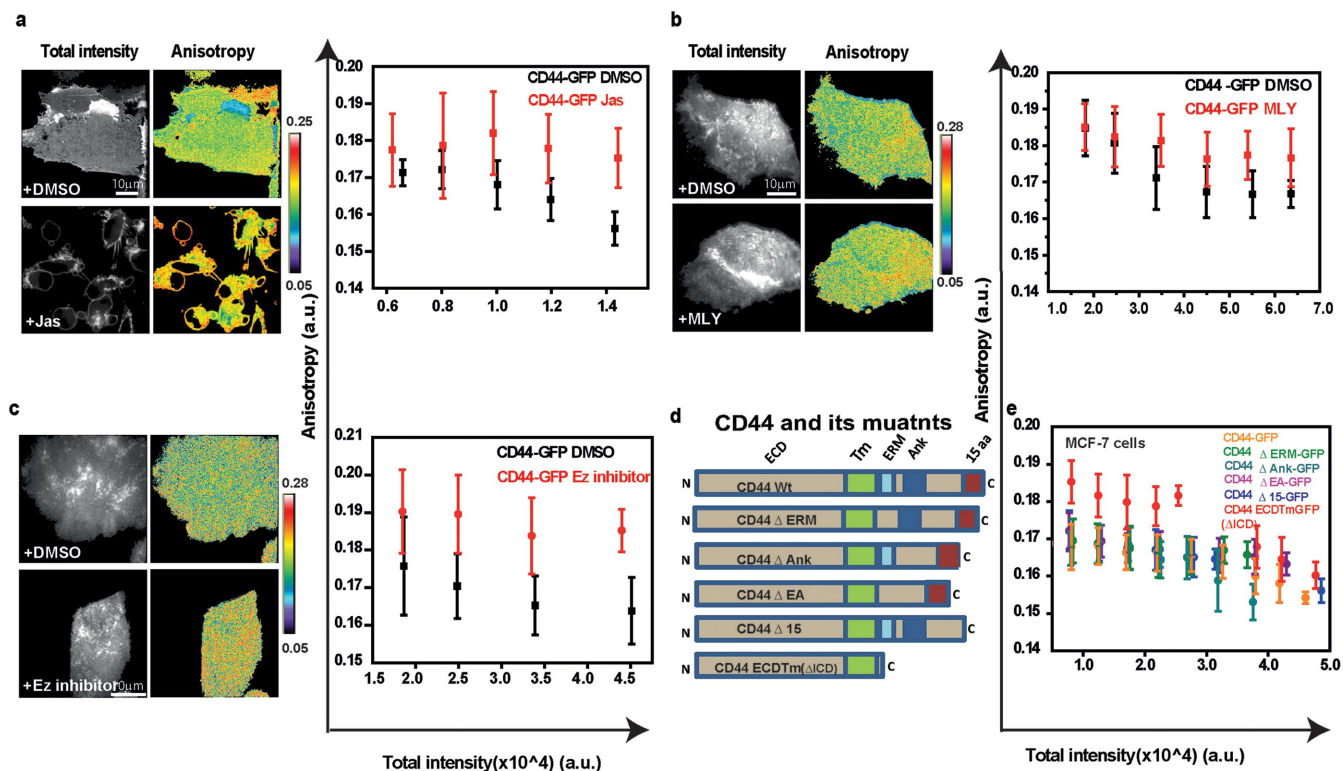


FIGURE 6: CD44 nanoclustering is regulated by the underlying actomyosin machinery. Total intensity and anisotropy images of cells expressing CD44-GFP (a–c) expressed in CHO cells, either untreated or treated with actin polymerization stabilizer, Jas (a, Jas; 14 μ M; 15 min; Con [n] = 10 fields, Treatment [n] = 22 fields), Myosin inhibition cocktail (b, MLY 20 μ M; 60 min; Con [n] = 20 fields, Treatment [n] = 26 fields), Ezrin inhibitor (c, 25 μ M; 60 min, Con [n] = 16 fields, Treatment [n] = 11 fields). Graphs show anisotropy values plotted against intensity collected from regions from the cells as detailed in experimental methods. In all conditions treatment with the indicated inhibitors show a significant difference in the recorded values of anisotropy ($p < 10^{-5}$). Difference between distributions has been tested for significance by Mann–Whitney tests. The data are from one representative experiment. Each experiment was conducted at least twice with similar results. (d) Schematic of CD44 and different deletion mutants for ezrin, ankyrin, and last 15 amino acids of the tail with the names of the constructs indicated next to its diagram. (e) Plot shows intensity vs. anisotropy distributions of the CD44 mutants in MCF-7 cells that exhibit low surface levels of CD44. (Distribution of anisotropy values were tested for significance using Mann–Whitney test and $p < 10^{-120}$ was obtained for CD44-GFP and CD44ECDTm-GFP; CD44-GFP [n] = 19 fields, CD44-ECDTm-GFP [n] = 15 fields, CD44- Δ 15GFP [n] = 16 fields, CD44- Δ ERM-GFP [n] = 13 fields, CD44- Δ EA-GFP [n] = 16 fields, CD44- Δ Ank-GFP [n] = 17 fields.)

membranes devoid of the dynamic actin cortex (Jaumouillé *et al.*, 2014). Fluorescence emission anisotropy of CD44-GFP on blebs of Jas-treated cells was higher compared with the flat membranes of untreated cells (Figure 6a). This also holds true for the CD44TmICD-GFP mutant, which is devoid of the ECD (Supplemental Figure S6a). These observations strongly suggest that the interactions with a dynamic actin cortex (absent in blebs) are a key determinant of nanoclustering of the protein at the cell surface. Moreover, treatment of cells with a cocktail of inhibitors (ML-7 and Y27632/ H11152) (Totsukawa *et al.*, 2000; Saha *et al.*, 2015) that inhibit myosin regulatory light chain phosphorylation of class II nonmuscle myosins, thereby inactivating them, resulted in a loss of nanoclustering of the CD44-GFP, as indicated by the increase in emission anisotropy of CD44-GFP compared with control cells (Figure 6b and Supplemental Figure S6c, where similar results are also obtained for the ECD-deleted mutant CD44TmICD-GFP). This result indicates that a dynamic actomyosin-driven mechanism facilitates nanoclustering of CD44 at the plasma membrane.

CD44 has been shown to associate with the actin cytoskeleton-binding proteins, ezrin and ankyrin (Bourguignon, 2008; Mrass

et al., 2008) while the last 15 amino acids of CD44 confer it the ability to interact with talin1, vinnexin, LMO1, and IQGAP1, all of which are potential interactors of the actin cytoskeleton as well as multiple other proteins (Skandalis *et al.*, 2010). To understand whether CD44 is associated with any particular adaptor protein that confers it with a cytoskeleton-sensitive clustering, we used two strategies: one where we perturbed the cytoskeletal coupling of CD44 using a small molecule inhibitor of ezrin function and the other using site-directed mutagenesis to specifically generate mutants that would be deficient in one or more actin-binding domains: CD44 Δ ERM (deletion of ezrin-binding site), CD44 Δ Ank (deletion of ankyrin-binding site), CD44 Δ EA (both the ezrin- and the ankyrin-binding sites are deleted), and CD44 Δ 15 (deletion of the last 15 amino acids) tagged to GFP on the cytoplasmic side (see Supplemental Table S1; Figure 6d).

When we inhibit ezrin function using the small molecule inhibitor of ezrin (NSC668394), it resulted in an increase of the fluorescence emission anisotropy of CD44 (Figure 6c), indicating the importance of ezrin function in CD44 nanoclustering. Similar effects were also observed for the CD44TmICD-GFP mutant (Supplemental Figure S6b). However, when we expressed the

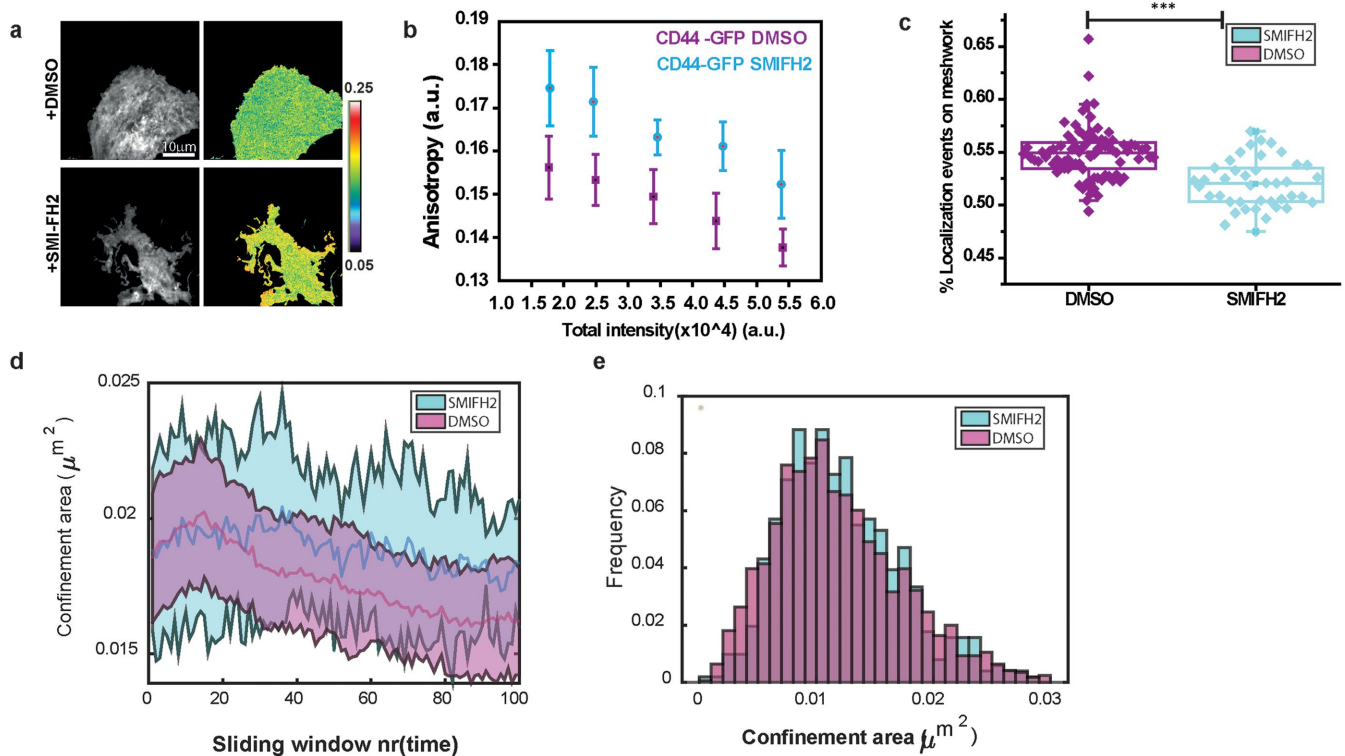


FIGURE 7: Formin-mediated actin polymerization affect nano- as well as meso-scale distribution and turnover of CD44. (a, b) Total intensity and anisotropy images of cells expressing CD44-GFP expressed in CHO cells treated with formin inhibitor (SMIFH2 for 30 min; Con [n] = 19 fields, Treatment [n] = 13 fields, $p < 10^{-5}$). (c) Plot describing fraction of localizations detected on the meshwork in control cells compared with formin inhibited condition ($p < e^{-8}$). (d) Plot depicting time evolution of meso-scale domains on vehicle (DMSO) vs. formin inhibitor treatment. The x-axis depicts time as 2 s sliding window (depicted as frame number) and the y-axis depicts confinement area. (e) Plot depicting confinement area of the mesoscale domains in formin-perturbed cells compared with untreated ones do not exhibit detectable differences. (DMSO [n] = 12 cells, SMIFH2 [n] = 9 cells).

various truncation mutants in cells, homo-FRET-based anisotropy measurements revealed a minimal difference in steady-state anisotropy distribution between the full-length receptor and the mutant proteins in MEFs, CHO cells (Supplemental Figure S7, a and a', respectively), and validated in COS-7 and MCF-7 cells (Supplemental Figure S7a'' and Figure 6e) to ensure that smaller differences in the nanoclustering of the mutants compared with the wild-type protein were also detected. This suggests that there are redundant ways of the mutant protein to associate with the actin-myosin machinery, and it is only when the entire cytoplasmic tail is deleted that this engagement is lost and nanoclustering is abrogated.

Meso-scale organization and turnover of CD44 is regulated by formin-nucleated actin dynamics

The diffusion of CD44 has been suggested to be sensitive to formin-generated actin filaments (Freeman *et al.*, 2018) since upregulation of Rho activity (which in turn regulates formin activity) influences the diffusion behavior of CD44. To test which actin nucleation machinery is responsible for CD44 nanoclustering, we inhibited formin- and Arp2/3-mediated actin filament-nucleation activity in CHO cells using small molecule inhibitors, SMI-FH2 and CK-666, respectively. CD44 nanoclustering was much more sensitive to inhibition of formin nucleation (Figure 7a) compared with Arp2/3 perturbation (Supplemental Figure S6d). These results indicate that formin-nucleated F-actin filaments not only influence the mobility of the receptor as reported previously (Freeman *et al.*, 2018) but importantly also pro-

motes its nanoclustering and, as a consequence, may also influence its meso-scale organization.

To ascertain the effect of formin perturbation on the meso-scale meshwork, we conducted high-density single particle imaging of SNAP-CD44-GFP, as described before, in COS-7 cells where we earlier elucidated the coexistence of nanoclusters with meso-scale domains. Our results indicate that meso-scale meshwork of CD44 is perturbed in formin-perturbed cells. Although the confinement area distribution is not significantly altered in formin-perturbed cells compared with vehicle (dimethylsulfoxide [DMSO])-treated cells (Figure 7e), the fraction of localization events detected along the meshwork in formin-inhibited cells (Figure 7, b–d) is significantly reduced, which is reminiscent of the distribution of the SNAP-CD44Tm-GFP that lacks both the cytoplasmic and the exoplasmic domains and is also defective in nanoclustering.

A striking difference in the formin-inhibited cells compared with the untreated cells was in the turnover time of the meso-scale domains. Time evolution analysis of the meso-scale domains revealed that while untreated (vehicle-treated) cells exhibited a visible disassembly/reorganization of the mesoscale domains, formin-inhibited cells exhibited a marked persistence of meso-scale domains (Figure 7d) during the observed time window. These results indicated that dynamic remodeling of the meso-scale meshwork is dependent on formin activity, consistent with the suggestion that formin-driven actin polymerization is a key contributor to dynamic remodeling of the actin meshwork (Fritzsche *et al.*, 2013).

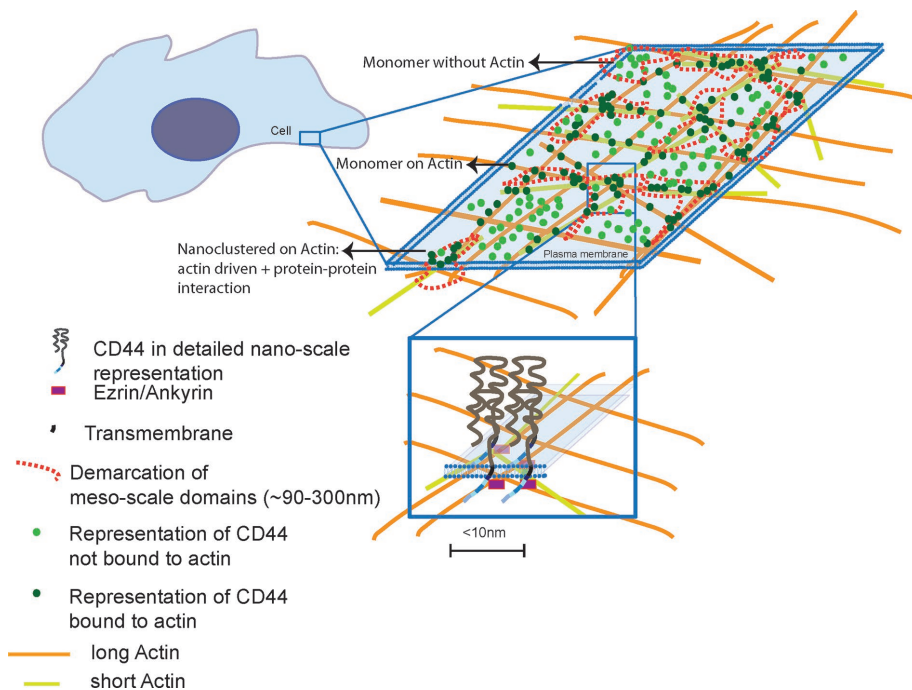


FIGURE 8: Proposed model for plasma membrane organization of CD44. In the cell membrane an ROI is outlined to show the distribution of monomers as well as clusters of CD44 receptors. Nanoclustered receptors are shown coupled to actin cytoskeletal elements by adaptors such as ezrin/ankyrin (see zoomed-in nanocluster) interspersed with unattached CD44 molecules. The clusters of receptors are depicted as being driven by the action of formin polymerized actin filaments and myosin driven actin motility (molecules not depicted in the schematic). The meso-scale domains are CD44 localization hotspots identified in our experiment that are characterized by their close association with nanoclusters of the protein. The emerging meso-scale meshwork of the cell membrane receptor (depicted by the orange dotted line) may reflect the cytoskeletal meshwork juxtaposed to the plasma membrane.

DISCUSSION

CD44 has a multitude of extracellular and cytoplasmic interactions that makes it an ideal candidate for studying regulation of the organization of a typical membrane protein. Here we have used noninvasive methods to study nanoclustering and dynamics of CD44 using live-cell compatible techniques such as homo-FRET imaging and SPT methods to generate spatial maps of the protein at the plasma membrane at the nano- and meso-scale. Previous studies have attempted to understand CD44 organization by multiple approaches, from characterizing graded distribution of GP-80 in motile fibroblasts (Ishihara *et al.*, 1988) to superresolution imaging wherein CD44 was found clustered at the cell membrane using STORM, and extracellular galectins were found responsible for their nanoclustering (Lakshminarayan *et al.*, 2014). In another study, the ICD was implicated in supporting mobile clusters at the membrane based on hetero-FRET measurements, brightness number analysis, and biochemical cross-linking studies in mammalian cells (Wang *et al.*, 2014). In a more recent study, SPT on CD44 revealed that CD44 diffusion is confined to pickets and fences and may indeed determine the corraling of other membrane proteins such as the FcγRIIA (Freeman *et al.*, 2018).

The results reported here provide a comprehensive understanding of the organization of CD44 by combining the determination of distribution and diffusion behavior of the protein across varying spatial scales at the plasma membrane of living cells. Cartography analysis (to probe the meso-scale organization of the protein) and its correlation with anisotropy measurements (reporting on nanoclus-

tering), for the first time, bridge the gap between SPT-based diffusion studies and the steady-state nanocluster detection method of homo-FRET. Complemented with the cartography analysis of single particle localizations and nanocluster distribution in STORM images, the combination of these approaches enabled us to build a hierarchical framework for the organization of a type-1 transmembrane protein at the plasma membrane (Figure 8). We find that actomyosin templated nanoclusters of CD44 spatially enrich the receptors along a meso-scale meshwork pattern, laid down by frequent localizations of the protein at the plasma membrane. These nanoclusters resemble actomyosin-based clusters observed for model transmembrane proteins with actin-binding domains (Chaudhuri *et al.*, 2011; Gowrishankar *et al.*, 2012).

The correlation between nano-scale and meso-scale organization of the protein and DC-SPT reconciles the apparent heterogeneity in diffusion modes of molecules to confinement driven by clustering at spatially separated domains on the plasma membrane. From our meso-scale organization and SPT studies, the regions on the membrane where the receptors are transiently confined/ temporarily arrested correspond to regions of receptor colocalization as well as potentially localization hotspots. These regions have an area ~100–300 nm, outlining a fragmented meshworklike pattern.

Moreover, the timescale of turnover of localization hotspots (Figure 7d) corresponds to the timescale of transient confinement of single molecules of CD44 (~few [< 3] s; Figure 2). The receptor transiently associates with such regions and eventually unbinds to diffuse again, often guided by the underlying actin cytoskeleton-laid fences, until it encounters another suitable site at the membrane-cytoskeleton interface to be arrested again. Thus, we propose that our localization hotspots could correspond to the picket fences described earlier (Murase *et al.*, 2004; Fujiwara *et al.*, 2016).

To ascertain whether actin dynamics-driven mechanisms could template the nano- and the meso-scale organization of CD44, we investigated the role of formin nucleation-based actin polymerization. As nanoclustering of CD44 is lost on formin perturbation, we also observe concomitant lowering of the CD44 localizations detected on the underlying meshwork. This is reminiscent of the Tm of CD44 (CD44Tm-GFP) that cannot bind to actin. Additionally the meso-scale domain turnover is remarkably slowed down. This is consistent with previous studies that implicate the role of formin activity in the turnover of the underlying cortical actin meshwork (Fritzsche *et al.*, 2013). These findings lead us to an important conclusion that meso-scale meshwork of CD44 arises as a consequence of the association of CD44 with the underlying actin cortex, and it is likely that the formin-mediated actin nucleation and turnover of the cortical actin meshwork contribute to the pool of dynamic actin necessary to template the nanoclustering of the protein as proposed previously (Chaudhuri *et al.*, 2011). This also provides a natural explanation for the enrichment of CD44 nanoclusters along the

meso-scale mesh, which appears to mirror the cortical actin cytoskeleton mesh. At this time it should be noted that further experiments are necessary to prove the relationship between the cortical actin meshwork and the mesoscale meshwork of CD44.

Nanoclustering of CD44 is also abrogated on removal of the cytoplasmic domain of CD44 (in Figure 3f). This finding is further supported by cytoskeletal sensitivity of nanoclustering of the protein. The sensitivity of CD44 nanoclustering particularly to formin and ezrin perturbation is well aligned with the changes in CD44 diffusion on similar perturbations, observed in SPT recently (Freeman *et al.*, 2018). In that study, formin- and ezrin-mediated picketing function of CD44 had been implicated in regulating FcγRIIA dynamics and function in phagocytosis. Involvement of similar molecular machinery in nanoclustering, as reported here, strongly suggests that the picketed CD44 receptors are nanoclustered by the underlying dynamic actin filaments generated as a consequence of formin-driven actin polymerization, and driven by myosin activity.

In this study, we have attempted to gain insights into specific interactions mediated by the ECD and ICD of CD44 in determining its diffusion and organization at the cell membrane. We find a strong correlation between nanoclustering potential and the tethering strength for the different truncation mutants of CD44 at the cell surface. Although removal of the ECD has little effect on the confinement radius of CD44, removal of the ICD from the mutant already lacking the ECD (CD44Tm-GFP) has a stronger effect on its confinement as well as localization on the meshwork at the mesoscale (Figures 4d and 5, b and d). The ICD thus emerges as a stronger determinant for tighter confinement of CD44 at the membrane and as the domain that augments the registry of the mesoscale distribution with a meshwork pattern. Together with the result suggesting that the ECD deleted mutant still exhibits acto–myosin-sensitive nanoclustering (Supplemental Figure S6), we believe that the mesoscale organization is templated on an underlying cortical actin mesh and serves to orchestrate the emergence of transient nanoclusters in its proximity.

The meshwork pattern that we observe may have a larger significance, since SNAP-CD44Tm-GFP and SNAP-CD59-GPI, proteins that are not directly coupled to actin, also exhibit a meshworklike appearance at the meso-scale. FcγRIIA, which cannot interact with actin but associates with a CD44 defined mesh (Freeman *et al.*, 2018), also exhibits a spatially restricted diffusion pattern and non-random diffusion at the meso-scale. This is likely to be mediated via lateral association of their membrane anchoring domains with actin-binding membrane pickets, or confinement within membrane compartments demarcated by picketing proteins. These data support the picture of a tightly coupled actin-membrane composite where even proteins that do not couple to actin are impacted by the patterning of the underlying meshwork.

With further sophistication of imaging and analysis methods, the correlation of cartography and anisotropy can be studied with higher temporal resolution. While our study is currently restricted to cytoskeletal interactions of CD44, there remains scope for detailed analysis of the influence of the exo-plasmic interactions with molecules such as galectins and HA. Simultaneous imaging of signaling and cytoskeletal adaptors along with CD44 can open up possibilities for exploring potential outside-in (ligand binding can lead to signaling adaptor recruitment) as well as inside-out signaling (ankyrin binding can influence hyaluronic acid binding; Zhu and Bourguignon, 2000) at the nano- and meso-scale domains. Since CD44 is implicated in processes such as metastasis, phagocytosis, or lymphocyte rolling (Hill *et al.*, 2006; Vachon *et al.*, 2006; Donatello *et al.*, 2012; Hanke-Roos *et al.*, 2017), they provide physiologically

relevant scenarios where local and global organization of CD44 may have an impact on relevant physiological scenarios.

We believe that the spatial organization of CD44, determined by the dynamic remodeling of the actin cytoskeleton, defines dynamic fences that partition the receptor in different regions of the cell membrane. These fences have been implicated in the phagocytic function of FcγRIIA and the endocytosis of DC-Sign receptor, which are receptors that do not exhibit direct interaction with the actin cytoskeleton (Torreno-Pina *et al.* 2014; Freeman *et al.* 2018). In conclusion, our approach and findings provide a multiscale view of organization of a transmembrane protein at the cell membrane, revealing a hierarchical framework where actomyosin-driven nanoclusters emerge in close association with an underlying dynamically remodeling meso-scale meshwork, enabling the cells to spatiotemporally regulate receptor organization.

EXPERIMENTAL METHODS

Plasmids, cell lines, and antibodies

CD44-GFP, CD44ECDm-GFP, and CD44TmICD-GFP cloned in p-EGFP N1 vector were gifts from Rob Parton at the University of Queensland, Australia. CD44ΔERM-GFP, CD44ΔAnk-GFP, CD44ΔEA-GFP, and CD44Δ15-GFP constructs were generated by site-directed mutagenesis using CD44-GFP as the template in the same backbone. SNAP- and FR-tagged CD44 constructs were designed and cloned into a lentiviral pHR transfer backbone and cloned between *MluI* and *BamHI/NotI* sites using the Gibson Assembly method. All constructs were sequenced and verified using appropriate primers (Supplemental Table S1). SNAP CD59 GPI was obtained from Addgene (Addgene #50374). Sequences and primer sequences will be made available on request. Cell line-expressing FR-CD44TmICD and FR-CD44Tm were generated by transfecting and selecting transfected cells by staining for FR-expressing cells with anti-FR MOV19 antibody using fluorescence-assisted cell sorting. CHO cells were cultured in Ham's F12 media (HiMedia, Mumbai, India); MCF-7, COS-7 (African green monkey kidney cells), and MEFs were cultured in DMEM high glucose (Gibco, 21720-024). The media was supplemented with fetal bovine serum (FBS) (Gibco, 16000044) and a cocktail of penicillin, streptomycin, and L-glutamine (Sigma; G1146-100 ml). MEFs, MCF-7, COS-7, or CHO cells were seeded sparsely and grown for 2 d on 35-mm cell culture dishes fitted with a glass bottom coverslip for imaging. Cells were transfected with the different CD44 plasmids, 12–16 h before imaging, using FuGENE 6 Transfection Reagent (E2692; Promega).

Antibody labeling and expression level estimation

Endogenous and overexpressed CD44 on the cell surface in the different cell lines, plated on cover slip bottom 35-mm dishes, after 2 d of plating, were labeled using IM7 antibody (14-0441-82; eBioscience) on ice for 1 h followed by incubation with anti-Rat secondary antibody tagged to Alexa 633 (A21094; Life Technologies) on ice for 1 h. The antibodies were diluted in 10% FBS containing culture media (DMEM). The cells were washed and imaged in HEPES buffer and imaged using a 20× objective on a spinning-disk microscope. Mean intensity from ROIs drawn around cells was quantified using ImageJ.

Actomyosin perturbation

Blebs were generated using 14 μM Jas (Thermo Fisher, Invitrogen; Cat. No. J7473) for 15 min. Formin perturbation was carried out using 10–25 μM SMI-FH2 (Calbiochem; Cat. No. S4826-5MG) for 15 min–1 h based on experimental requirement. Arp2/3 inhibition was carried out using 200 μM CK-666 (Sigma-Aldrich; Cat. No. SML0006 5MG) treatment for 3 h. Ezrin perturbation was carried out

using the inhibitor NSC668394 purchased from EMD Millipore (Cat. No. 341216-10MG). Cells were treated with 25 μ M of the drug for 1 h. Myosin II perturbation was carried out using a cocktail of ML-7 (Sigma-Aldrich; Cat. No. I2764) and Y27632 (Sigma-Aldrich; Cat. No. Y0503-1MG) or H1152 purchased from Tocris (Cat. No. 2414). Cells were treated with a cocktail of the ML-7 and Y27632/ H1152 at a final concentration of 20 μ M of each for 1 h. Owing to the reversible nature of the drugs acting on the target, imaging was carried out in the presence of the drug except in the case of Jas treatment. All drug treatments were carried out in HEPES buffer saline containing 2 mg/ml glucose at 37°C for the indicated time periods.

STORM sample preparation and imaging

CHO cells were plated on an eight-well Lab-Tek #1 chamber slide system (Nunc) at a density of 30,000 cells/well. Cells were incubated at 37°C for 24 h. After incubation, the samples were fixed with 4% paraformaldehyde in phosphate-buffered saline (PBS) at room temperature for 20 min. After fixation, blocking solution (3% wt/vol bovine serum albumin in PBS) was applied for 30 min. Cells were labeled with rat-anti-mouse-anti-CD44 primary antibody (Clone KM114; BD Pharmingen #558739) at a concentration of 5 μ g/ml for 1 h at room temperature. The corresponding secondary antibody (anti-rat) was tagged with Alexa Fluor 647 (Invitrogen) as a reporter and with Alexa Fluor 405 as an activator. The secondary antibody was incubated for 1 h at room temperature. Cells were stored in 1% PFA in PBS. The STORM buffer used was the same as that of Gómez-García *et al.* (2018): Glox solution (40 mg/ml Catalase [Sigma Aldrich], 0.5 mg/ml glucose oxidase, 10% glucose in PBS) and MEA 10 mM (Cysteamine MEA [Sigma-Aldrich; #30070-50G] in 360 mM Tris-HCl). The imaging for STORM on endogenous CD44 from top surface in CHO cells is from one experiment.

To study the nearest-neighbor distribution of clusters, we identified the clusters of localizations based on intensity (i.e., high density of localizations) and determined the position of the center of mass. With this information, we calculate the NND for the experimental set. For the simulations, we take the same identified clusters (keeping their size) and reshuffle them in space. We repeat this process many times (100x) to get more robust information on the simulated NND.

Live cell imaging for fluorescence emission anisotropy and cartography experiments

All live imaging were interchangeably carried out, based on requirement, in one of the following setups: 1) confocal spinning disk microscope (for imaging blebs in 3D) equipped with a Yokogawa CSU-22 unit and 100x, 1.4NA Nikon oil objective; Andor technologies laser combiner emitting 488 and 561 nm wavelengths, amongst others; and Andor ixon+897 EMCCD cameras. Images were acquired using Andor iQ2 software. 2) Total internal reflection fluorescence (TIRF) microscope setup was equipped with Nikon Eclipse Ti body; a 100x, 1.45NA Nikon oil objective; photometrics Evolve EMCCD cameras; an Agilent laser combiner MCL400 (Agilent Technologies) whose 488, 561, and 640 nm excitation wavelengths were used as necessary; and μ Manager for image acquisition. 3) TIRF microscope setup was equipped with Nikon TE2000 body; a 100x, 1.49NA Nikon oil objective; EMCCD Cascade 512 cameras (Photometrics, Tuscon, AZ); a home-built laser combiner equipped with 488 and 561 nm lasers; and Metamorph/ μ Manager for image acquisition. Wherever necessary, live imaging was performed in a temperature-controlled stage-top incubator chamber with immersion thermostat, ECO Silver, from Lauda Brinkmann.

Fluorescence emission anisotropy measurements

We measure emission anisotropy of our protein of interest by labeling them with GFP or PLB, both of which are suitable for fluorescence anisotropy measurement to report on Homo-FRET (Sinnecker *et al.*, 2005; Ghosh *et al.*, 2012). Cells were treated with 50–100 μ g/l cycloheximide in complete media for 2.5–3 h prior to imaging for anisotropy measurement of GFP-based constructs, in order to prevent signal from GFP from the ER/Golgi-based internal pool contaminating the fluorescence signal from the plasma membrane pool. This is in accordance with anisotropy measurements of GFP-tagged membrane proteins conducted in the lab in the past (Sharma *et al.*, 2004). Cells were imaged in HEPES buffer containing 2 mg/ml glucose on an inverted TIRF microscope using a polarized excitation light source. Emission was split into orthogonal polarization components using a polarization beam splitter and collected simultaneously by two EM CCD cameras to detect polarization of emitted fluorescence. Fluorescence emission anisotropy measurements were interchangeably carried out, based on requirements, in one of the dual camera-equipped imaging systems described before. Steady-state fluorescence emission anisotropy was calculated as elaborated in Ghosh *et al.* (2012). The absolute value of anisotropy is a function of the effective numerical aperture of the imaging system (Ghosh *et al.*, 2012). Since the effective numerical aperture is determined by the combinatorial effect of individual lenses in the light path of the microscope system, the absolute anisotropy value of the same protein varied from one system to another. Also, since the different experiments reported here have been conducted over several years, absolute values of anisotropy for the same constructs would have varied based on the status of the optics in a given microscope system. Hence, the measurements typically contained an internal control for sensitivity of anisotropy change, which was generally a measurement of the extent of anisotropy change between the wild-type CD44-GFP and CD44ECDTm-GFP (or CD44-TmICD-GFP and CD44-Tm-GFP).

Fluorescence anisotropy image analysis

Image analysis was carried out using imaging software: ImageJ or Metamorph. Fluorescence emission anisotropy of GFP- and PLB-tagged proteins was calculated using images from the two cameras, which were individually background corrected, and the perpendicular image was additionally G-Factor corrected (Ghosh *et al.*, 2012) to rectify effects of inherent polarization bias of the imaging system. Regions of interest (ROIs) of size 20 \times 20 or 30 \times 30 pixels were drawn to sample the cell membrane, and anisotropy values from these regions were obtained. Anisotropy maps were generated after aligning the images from the two cameras and calculating pixelwise anisotropy value as described in Ghosh *et al.* (2012) using a custom code written in MATLAB (MathWorks, Natick, MA). Code will be available on request. For data plotting, intensity was binned for appropriate intensity range, and each data point represents mean, and an error bar represents SD of anisotropy corresponding to the intensity bin. We ensured that data comparisons were done between conditions across similar intensity ranges. Intensity range chosen was decided based on different microscope properties, especially the bit depth and noise levels of the cameras. For representation calculated anisotropy values from the intensity images of the parallel and perpendicular cameras have been plotted on the y-axis as a function of the expression level, which is described as "Total intensity in arbitrary units" on the x-axis. Here, the total intensity is computed as a summation of the intensity recorded in the parallel image and two times the intensity recorded in the perpendicular image as described in Ghosh *et al.* (2012).

Labeling of SNAP-tagged CD44 membrane receptors

MEFS, COS-7, or CHO cells were seeded sparsely and grown for 2 d on 35-mm cell culture dishes fitted with a glass coverslip at the bottom. Cells were transfected with the different SNAP-tagged CD44 plasmids 16–18 h prior to the experiment using FuGENE 6 Transfection Reagent. Labeling was done with SNAP tag-specific photo-stable fluorescent probes, SNAP Alexa 546, SNAP-surface 549 ($\lambda_{ex}/\lambda_{em}$: 560/575 nm, purchased from New England Biolabs, Ipswich, MA), or JF646-SNAP ligand ($\lambda_{ex}/\lambda_{em}$: 646/664 nm) by incubating for 10 min at 37°C using a dilution of 30 nM (for single particle experiments) and 50–100 nM (for cartography experiments) with 10% serum containing F12 medium and then washed extensively with glucose-M1 buffer (150 mM NaCl, 5 mM KCl, 1 mM CaCl₂, 1 mM MgCl₂, 20 mM HEPES, pH 7.3; supplemented with D-glucose at 2 mg/ml) to get rid of free dyes. The dyes were chosen to ensure they are spectrally different from GFP with minimum bleed-through. Dual color labeling was done with JF549-cpSNAP ligand ($\lambda_{ex}/\lambda_{em}$: 549/571 nm) and JF646-SNAP ligand ($\lambda_{ex}/\lambda_{em}$: 646/664 nm) fluorophores by incubating for 10 min at 37°C with F12 serum medium at mixed concentrations of 50 and 150 nM for the respective dyes. Singly or dually labeled cells were subsequently washed and imaged at 37°C in the presence of HEPES buffer containing 2 mg/ml glucose.

SPT

Video imaging of single fluorescent receptors on cell membranes was performed using a home-built, TIRF microscope equipped with a Nikon Eclipse Ti body and a Nikon 100× Apochromat 1.49 NA objective, with a C-MOS sensor-based high-speed camera (FASTCAM-SA1; Photron, Tokyo, Japan; Shibata *et al.*, 2012; Hiramoto-Yamaki *et al.*, 2014; Komura *et al.*, 2016) coupled to a two-stage microchannel plate intensifier (C8600-03; Hamamatsu Photonics, Hamamatsu, Japan) by way of an optical-fiber bundle. Single molecules were observed at 16.7 ms (60 fps) temporal resolution with an excitation laser of 561 nm of power density ~2.43 kW/cm², with a FWHM (full-width-half-maximum) of 333 ± 13 nm and a pixel size of 54 nm, in the presence of an additional 1.5× lens in front of the camera. The localization precision was estimated to be ± 28 nm. The precision was measured after immobilizing CD44 labeled with SNAP-surface 549 fluorescent probe, on MEFS cells, by fixing the cell membranes with 4% paraformaldehyde and 0.1% glutaraldehyde for 60 min at room temperature (Tanaka *et al.*, 2010). The precision was determined by fitting the centroid position from single molecules using a 2D Gaussian function and calculated from radial SD $\delta_r = (\delta_x * \delta_y)^{1/2} \approx \delta_x \approx \delta_y$ of x- and y-coordinates over time. Tracking of membrane molecules (x- and y-coordinates) was determined using C++ based computer program as described previously (Fujiwara *et al.*, 2002; Koyama-Honda *et al.*, 2005). The mean-squared displacement (MSD) for every time frame for each trajectory was calculated as per the following equation:

$$\text{MSD}(n,\Delta t) = \frac{1}{N-n-1} \sum_{j=1}^{N-n-1} \left[x(j\Delta t + n\Delta t) - x(j\Delta t) \right]^2 + \left[y(j\Delta t + n\Delta t) - y(j\Delta t) \right]^2 \quad (1)$$

where Δt is the time increment, N is the number of frames of the trajectory, n is the number of time increments, and x and y represent the particle coordinates. Then, the microscopic diffusion coefficients (D_{2-5}) of individual trajectories were calculated through a linear fit performed at short time lags ($n = 2-5$) using the equation

$$\text{MSD}(n,\Delta t) = 4D_{2-5}t + \Delta_0 \quad (2)$$

where the MSD intercept at zero time lag, Δ_0 , is associated to the localization precision.

Mobile fractions and temporal confinement detection

Temporal confinement or temporary arrest of lateral diffusion (TALL) was analyzed defining parameters of detection circular radius and threshold residence time by using the algorithm developed by Sahl *et al.* (2010). Theoretically, simulated randomly diffusive trajectories show false TALL of ~5% of total trajectory lengths. Therefore, the detection of circular radius was set, based on calculating average diffusion coefficient (0.3 $\mu\text{m}^2/\text{s}$) of mobile fractions of CD44 and probability of temporal confinement <5% during Brownian motion within 10 frames of A 16.7-ms exposure. In the escape probability method, the probability $P(r, t)$ that a particle diffusing with the diffusion coefficient D , remains confined within the circle of radius r and the time interval t can be expressed as

$$P(r, t) = 1 - \exp\left(\frac{-r^2}{4Dt}\right) \quad (3)$$

Data represented are pooled from two different replicates, which individually exhibited similar trend. Choice of cells from which data have been represented was made based on optimal labeling density and flatness of membrane morphology since imaging has been done in the TIRF mode.

Analysis was extended to determine the discrete probability density $P(\Delta r^2, \Delta t)$ by cumulative square displacements, which will represent a sequence of spatial positions $\vec{r}(t)$ separated by variable time lags Δt . The cumulative probability $P(\Delta r^2, \Delta t)$ is defined by Eq. 3, where α is the time fraction of characteristic free diffusion with coefficient D , $r_{\text{trap}} = (\bar{r}_{\text{trap}}^2 - \sigma_r^2)^{1/2}$ corresponds to the trapping radius of the particle, and σ_r is the experimental localization error (Sahl *et al.*, 2010):

$$P(\Delta r^2, \Delta t) = \alpha \left[1 - \exp\left(\frac{-\Delta r^2}{4\sigma_r^2 + 4D\Delta t}\right) \right] + (1-\alpha) \left[1 - \exp\left(\frac{-\Delta r^2}{4\bar{r}_{\text{trap}}^2}\right) \right] \quad (4)$$

Probability density $P(\Delta r^2, \Delta t)$ observing for long steps was corrected with overlap integral of two circles with radius R by $P_{\text{track}}(\Delta r, R)$ as described in Sahl *et al.* (2010). Here we computed $P(\Delta r^2, \Delta t)$ with increments $\Delta(\Delta t) = 16.7$ ms and $\Delta(\Delta r^2) = 50$ nm².

Dual color trajectory analysis

Intermolecular separation distance between CD44 molecules labeled with JF549 (green) and JF646 (red) dyes was determined from the centroid locations of their dual color pair trajectories within boundaries ranging from 25 to 500 nm radius using C++ based computer program WinCol (Koyama-Honda *et al.*, 2005). Measurements were done with excitation lasers of 561 and 642 nm of power density ~2.43 and ~4.06 kW/cm², respectively, and detecting signals simultaneously by two cameras after splitting emission signals using a 561/647 dichroic mirror (Chroma Technology; 625DCXR) with corresponding emission band pass filters 593 ± 43 nm and 685 ± 40 nm. Localization accuracy of JF549 and JF646 dyes is ±29 nm and ±33 nm, respectively, while pixel size at image plane is 54 nm. Videos of the flipped green channel were used to generate randomly encountered colocalizations. Colocalization was defined when intermolecular distances were ≤200 nm for a minimum of three consecutive frames. The displacement between colocalized frames was then calculated. The displacement and step-size distribution were thereafter compared with transiently confined frames,

trajectories of mobile fractions, and all frames. Photobleaching analysis from individual spots of fluorophores did not reveal any significant bleaching in the timescale reported for the lifetime of colocalization of the protein (Supplemental Figure S2d). Data represented are pooled from two different replicates, which individually exhibited a similar trend. Choice of cells from which data have been represented was made based on optimal labeling density and flatness of membrane morphology since imaging has been done in TIRF mode. Total number of trajectories analyzed: SNAP-CD44-GFP = 27856, SNAP-CD44Tm-GFP = 7516.

Generation of cartography

Cartography maps were generated from movies (1000 frames, 10 fps) recorded in TIRF mode, as explained in the previous section, using subsaturation labeling conditions (50–100 nM). Identification of single molecules essentially corresponds to the identification of individual fluorescent spots at each given time frame. For this, we apply two criteria: First, the spots should have a size that is limited by diffraction, that is, this corresponds to the PFS of the microscope. Second, the intensity of each spot should be higher than the surrounding background. The localization precision of each individual spot is given by the number of counts on that spot, which in the case of our videos corresponds to ~20 nm. The spatial (x , y) coordinates of the labeled membrane receptors (for each of the constructs investigated) were thus retrieved from each frame using a MATLAB routine based on that of Crocker and Grier (1996), with subpixel accuracy. Finally, all the receptor coordinates of all frames were collapsed into a single image, the so-called cartography map. With this approach, one not only can access the nano-scale organization of the labeled receptor but also can access the mesoscale organization without the need of reconnecting trajectories (Torreno-Pina *et al.*, 2014). Cartography maps were also generated in different time windows, typically by integrating the localizations over 40 (Figure 2) or 20 frames (Figures 1e and 5). Experiments to obtain cartography maps of the receptor and the mutants have been conducted at least twice in MEFs and once in COS-7 cells. Formin perturbation and mesoscale organization imaging has been done at least twice and the represented experiment here is done in COS-7 cells. SNAP-CD44-GFP cartography in CHO cells and GPI mesoscale organization experiment has been conducted once.

Analysis of the cartography maps

Since the cartography maps are generated from localizations obtained as a function of time, their evolution is dynamic. Therefore, we restricted our analysis to time windows of 2 s by collapsing all the localizations from sequential 20 frames into a single, less crowded cartography image. Confinement areas were identified using the MATLAB routine DBSCAN (density-based spatial clustering of applications with noise) with settings ($\epsilon = 1.0$ and $\text{MinPts} = 10$). Finally, we defined the confinement area as the area occupied by a cluster of localizations.

For the time-evolution analysis of the meso-scale domains, the time windows correspond to 2 s, that is, 20 frames. Initially, clusters are defined at the time window 0 (frames within f_0 and $f_0 + 19$). Then, since we slide the window through the cartography map, at each time window we move 100 ms in the cartography.

Analysis of the interleaved anisotropy and cartography maps

To compare the cartography maps with the anisotropy images, we performed interleaved anisotropy imaging together with high-density SPT generating one anisotropy image before starting SPT, a

second anisotropy at frame 500 of the SPT recording, and a final one once the SPT recording was finished (after frame 1000). To reduce temporal variations on both the anisotropy and the cartography maps, we focused on anisotropy images at the corresponding frame 500 of the SPT movie. The anisotropy image was divided into small ROIs (22 × 22 pixels, with a pixel size of 106 nm). This was done in order to select only those regions where the plasma membrane is completely flat and therefore the anisotropy arises exclusively from the lateral distribution of the labeled receptors. In addition to this, for each ROI, we classified each pixel of the anisotropy map into three groups: low anisotropy (Low A), median anisotropy (Medium A), and high anisotropy (High A).

We then took the localizations between frames 480 and 520 of the SPT movie and generated a cartography map for each of the ROIs. We identified the clusters of localizations using the MATLAB routine DBSCAN with settings ($\epsilon = 1.0$ and $\text{MinPts} = 10$). With the localizations belonging to clusters, we assigned to each of them an anisotropy value corresponding to their location in the anisotropy ROI and classified them within the three groups. Simultaneously, we randomly distributed the same number of localizations on the anisotropy ROIs and also assigned their corresponding anisotropy value and posterior classification. Comparative anisotropy-cartography analysis has been done from an experiment with COS-7 cells where localization and GFP-based FRET information was obtained using dual cameras at specific intervals during acquisition of single molecule localization time series of the SNAP tag fluorophore.

Statistical analysis

Differences in anisotropy distributions between control and treatment were tested using a nonparametric Mann–Whitney test or KS test. The number of fields/cells imaged is mentioned for each experiment. The anisotropy and cartography data shown here are from one representative experiment. Each experiment was conducted at least twice unless otherwise mentioned. Quantification from cartography and SPT experiments was tested for significance using the Kruskal–Wallis test along with the post hoc Tukey–Kramer test and the Wilcoxon sum rank test of MatLab unless otherwise mentioned. In the figures, ns indicates no statistically significant difference between two populations. * indicates $p < 0.05$, ** indicates $p < 0.005$, *** indicates $p < 0.0005$.

ACKNOWLEDGMENTS

We thank Rob Parton for sharing with us the CD44-GFP, CD44ECDTm-GFP, and CD44TmICD-GFP constructs, which were originally used in Mrass *et al.* (2008). The JF dyes used in SPT studies were a generous gift from Luke Lavis, HHMI Janelia Research Campus. We thank Suvrajit Saha for contributions to the initiation of the project. We thank the Central Imaging and Flow facility of the National Centre for Biological Science for enabling us to use their equipment and Divya Gowda and H. Krishnamurthy for their help. We thank Marcus J. Taylor for helping in reagent development pertaining to the SNAP-tagged constructs. We thank Chaitra Prabhakara and Sanjeev Sharma for help with data representation, revision, and editing the manuscript. M.F.G.-P. acknowledges funding from the Fundació Privada Cellex, Generalitat de Catalunya through the Centres de Reserca de Catalunya program, Spanish Ministry of Economy and Competitiveness (“Severo Ochoa” Programme for Centres of Excellence in R&D [SEV – 2015 –0522] and FIS2017-89560-R) and from European Union H2020-ERC grant 788546-NANO-MEMEC. N.M. acknowledges funding from the European Union H2020 under Marie Skłodowska-Curie grant 754558-PREBIST. C.M. acknowledges funding from the Spanish

Ministry of Economy and Competitiveness and the European Social Fund through the “Ramón y Cajal” program 2015 (grant RYC-2015-17896), the “Programa Estatal de I+D+i Orientada a los Retos de la Sociedad” (grant BFU2017-85693-R), and the Generalitat de Catalunya (AGAUR Grant 2017SGR940). A.K. acknowledges support in part by grants-in-aid for scientific research Kiban S (16H06386) from the Japan Society for the Promotion of Science. TK.F. acknowledges grants-in-aid for scientific research from the Japan Society for the Promotion of Science (Kiban B [16H04775]). K.S. acknowledges grants-in-aid for scientific research from the Japan Society for the Promotion of Science (Kiban B [18H02401]). S.M. acknowledges a JC Bose Fellowship from the Department of Science and Technology, Government of India, a collaborative grant from the Human Frontiers Science Program (RGP0027/2012 with M.F.G.-P.), and a Wellcome Trust–Department of Biotechnology, Alliance Margadarshi fellowship (IA/M/15/1/502018).

REFERENCES

- Beck-García K, Beck-García E, Bohler S, Zorzin C, Sezgin E, Levental I, Alarcón B, Schamel WWA (2015). Nanoclusters of the resting T cell antigen receptor (TCR) localize to non-raft domains. *Biochim Biophys Acta* 1853, 802–809.
- Bourguignon LYW (2008). Hyaluronan-mediated CD44 activation of RhoGTPase signaling and cytoskeleton function promotes tumor progression. *Semin Cancer Biol* 18, 251–259.
- Chaudhuri A, Bhattacharya B, Gowrishankar K, Mayor S, Rao, M (2011). Spatiotemporal regulation of chemical reactions by active cytoskeletal remodeling. *Proc Natl Acad Sci USA* 108, 14825–14830.
- Clark PJ, Evans FC (1954). Distance to nearest neighbor as a measure of spatial relationships in populations. *Ecology* 35, 445–453.
- Crocker JC, Grier DG (1996). Methods of digital video microscopy for colloidal studies. *J Colloid Interface Sci* 179, 298–310.
- Donatello S, Babina IS, Hazelwood LD, Hill ADK, Nabi IR, Hopkins AM (2012). Lipid raft association restricts CD44-ezrin interaction and promotion of breast cancer cell migration. *Am J Pathol* 181, 2172–2187.
- Freeman SA, Vega A, Riedl M, Collins RF, Ostrowski PP, Woods EC, Bertozzi CR, Tammi MI, Lidke DS, Johnson P, et al. (2018). Transmembrane pickets connect cyto- and pericellular skeletons forming barriers to receptor engagement. *Cell* 172, 305–317.e10.
- Fritzsche M, Lewalle A, Duke T, Kruse K, Charras, G (2013). Analysis of turnover dynamics of the submembranous actin cortex. *Mol Biol Cell* 24, 757–767.
- Fujiwara T, Ritchie K, Murakoshi H, Jacobson K, Kusumi A (2002). Phospholipids undergo hop diffusion in compartmentalized cell membrane. *J Cell Biol* 157, 1071–1081.
- Fujiwara TK, Iwasawa K, Kalay Z, Tsunoyama TA, Watanabe Y, Umemura YM, Murakoshi H, Suzuki KG, Nemoto YL, Morone N, et al. (2016). Confined diffusion of transmembrane proteins and lipids induced by the same actin meshwork lining the plasma membrane. *Mol Biol Cell* 27, 1101–1119.
- García-Parajo MF, Cambi A, Torreno-Pina JA, Thompson N, Jacobson K (2014). Nanoclustering as a dominant feature of plasma membrane organization. *J Cell Sci* 127, 4995–5005.
- Gerecht S, Burdick JA, Ferreira LS, Townsend SA, Langer R, Vunjak-Novakovic G (2007). Hyaluronic acid hydrogel for controlled self-renewal and differentiation of human embryonic stem cells. *Proc Natl Acad Sci USA* 104, 11298–11303.
- Ghosh S, Saha S, Goswami D, Bilgrami S, Mayor S (2012). Dynamic imaging of homo-FRET in live cells by fluorescence anisotropy microscopy. *Methods Enzymol* 505, 291–327.
- Gómez-García PA, Garbaciak ET, Otterstrom JJ, García-Parajo MF, Lakadamyali M (2018). Excitation-multiplexed multicolor superresolution imaging with fm-STORM and fm-DNA-PAINT. *Proc Natl Acad Sci USA* 115, 12991–12996.
- Goswami D, Gowrishankar K, Bilgrami S, Ghosh S, Raghupathy R, Chadda R, Vishwakarma R, Rao M, Mayor S (2008). Nanoclusters of GPI-anchored proteins are formed by cortical actin-driven activity. *Cell* 135, 1085–1097.
- Gowrishankar K, Ghosh S, Saha S, C Rumamol, Mayor S, Rao M (2012). Active remodeling of cortical actin regulates spatiotemporal organization of cell surface molecules. *Cell* 149, 1353–1367.
- Hanke-Roos M, Fuchs K, Maleschlijski S, Sleeman J, Orian-Rousseau V, Rosenhahn A (2017). CD44 mediates the catch-bond activated rolling of HEPG2 iso epithelial cancer cells on hyaluronan. *Cell Adh Migr* 11, 476–487.
- Hill A, McFarlane S, Mulligan K, Gillespie H, Draffin JE, Trimble A, Ouhitit A, Johnston PG, Harkin DP, McCormick D, et al. (2006). Cortactin underpins CD44-promoted invasion and adhesion of breast cancer cells to bone marrow endothelial cells. *Oncogene* 25, 6079–6091.
- Hiramoto-Yamaki N, Tanaka KAK, Suzuki KGN, Hirotsawa KM, Miyahara MSH, Kalay Z, Tanaka K, Kasai RS, Kusumi A, Fujiwara TK (2014). Ultrafast diffusion of a fluorescent cholesterol analog in compartmentalized plasma membranes. *Traffic* 15, 583–612.
- Hofman EG, Bader AN, Voortman J, van den Heuvel DJ, Sigismund S, Verkleij AJ, Gerritsen HC, van Bergen en Henegouwen PMP (2010). Ligand-induced EGF receptor oligomerization is kinase-dependent and enhances internalization. *J Biol Chem* 285, 39481–39489.
- Howes MT, Kirkham M, Riches J, Cortese K, Walser PJ, Simpson F, Hill MM, Jones A, Lundmark R, Lindsay MR, et al. (2010). Clathrin-independent carriers form a high capacity endocytic sorting system at the leading edge of migrating cells. *J Cell Biol* 190, 675–691.
- Ishihara A, Holifield B, Jacobson K (1988). Analysis of lateral redistribution of a plasma membrane glycoprotein-monoclonal antibody complex [corrected]. *J Cell Biol* 106, 329–343.
- Jaumouillé V, Farkash Y, Jaqaman K, Das R, Lowell CA, Grinstein S (2014). Actin cytoskeleton reorganization by Syk regulates Fcγ receptor responsiveness by increasing its lateral mobility and clustering. *Dev Cell* 29, 534–546.
- Jiang H, Peterson RS, Wang W, Bartnik E, Knudson CB, Knudson W (2002). A requirement for the CD44 cytoplasmic domain for hyaluronan binding, pericellular matrix assembly, and receptor-mediated endocytosis in COS-7 cells. *J Biol Chem* 277, 10531–10538.
- Klotzsch E, Schütz GJ (2013). A critical survey of methods to detect plasma membrane rafts. *Philos Trans R Soc Lond B Biol Sci* 368, 20120033.
- Knudson W, Bartnik E, Knudson CB (1993). Assembly of pericellular matrices by COS-7 cells transfected with CD44 lymphocyte-homing receptor genes. *Proc Natl Acad Sci USA* 90, 4003–4007.
- Komura N, Suzuki KG, Ando H, Konishi M, Koikeda M, Imamura A, Chadda R, Fujiwara TK, Tsuboi H, Sheng R, et al. (2016). Raft-based interactions of gangliosides with a GPI-anchored receptor. *Nat Chem Biol* 12, 402–410.
- Koyama-Honda I, Ritchie K, Fujiwara T, Iino R, Murakoshi H, Kasai RS, Kusumi A (2005). Fluorescence imaging for monitoring the colocalization of two single molecules in living cells. *Biophys J* 88, 2126–2136.
- Kusumi A, Ike H, Nakada C, Murase K, Fujiwara T (2005). Single-molecule tracking of membrane molecules: plasma membrane compartmentalization and dynamic assembly of raft-philic signaling molecules. *Semin Immunol* 17, 3–21.
- Kusumi A, Sako Y (1996). Cell surface organization by the membrane skeleton. *Curr Opin Cell Biol* 8, 566–574.
- Kusumi A, Suzuki KGN, Kasai RS, Ritchie K, Fujiwara TK (2011). Hierarchical mesoscale domain organization of the plasma membrane. *Trends Biochem Sci* 36, 604–615.
- Lakshminarayan R, Wunder C, Becken U, Howes MT, Benzing C, Arumugam S, Sales S, Ariotti N, Chambon V, Lamaze C, et al. (2014). Galectin-3 drives glycosphingolipid-dependent biogenesis of clathrin-independent carriers. *Nat Cell Biol* 16, 595–606.
- Martínez-Muñoz L, Rodríguez-Frade JM, Barroso R, Sorzano CÓS, Torreño-Pina JA, Santiago CA, Manzo C, Lucas P, García-Cuesta EM, Gutierrez E, et al. (2018). Separating actin-dependent chemokine receptor nanoclustering from dimerization indicates a role for clustering in CXCR4 signaling and function. *Mol Cell* 70, 106–119.e10.
- Mori T, Kitano K, Terawaki S, Maesaki R, Fukami Y, Hakoshima T (2008). Structural basis for CD44 recognition by ERM proteins. *J Biol Chem* 283, 29602–29612.
- Mrass P, Kinjyo I, Ng LG, Reiner SL, Puré E, Weninger W (2008). CD44 mediates successful interstitial navigation by killer T cells and enables efficient antitumor immunity. *Immunity* 29, 971–985.
- Murase K, Fujiwara T, Umemura Y, Suzuki K, Iino R, Yamashita H, Saito M, Murakoshi H, Ritchie K, Kusumi A (2004). Ultrafine membrane compartments for molecular diffusion as revealed by single molecule techniques. *Biophys J* 86, 4075–4093.
- Overton MC, Blumer KJ (2000). G-protein-coupled receptors function as oligomers in vivo. *Curr Biol* 10, 341–344.
- Pageon SV, Tabarin T, Yamamoto Y, Ma Y, Nicovich PR, Bridgeman JS, Cohnen A, Benzing C, Gao Y, Crowther MD, et al. (2016). Functional role of T-cell receptor nanoclusters in signal initiation and antigen discrimination. *Proc Natl Acad Sci USA* 113, E5454–E5463.

- Ponta H, Sherman L, Herrlich PA (2003). CD44: from adhesion molecules to signalling regulators. *Nat Rev Mol Cell Biol* 4, 33–45.
- Saha S, Lee I, Polley A, Groves JT, Rao M, Mayor S (2015). Diffusion of GPI-anchored proteins is influenced by the activity of dynamic cortical actin. *Mol Biol Cell* 26, 4033–4045.
- Sahl SJ, Leutenegger M, Hilbert M, Hell SW, Eggeling C (2010). Fast molecular tracking maps nanoscale dynamics of plasma membrane lipids. *Proc Natl Acad Sci USA* 107, 6829–6834.
- Senbanjo LT, Chellaiiah MA (2017). CD44: A multifunctional cell surface adhesion receptor is a regulator of progression and metastasis of cancer cells. *Front Cell Dev Biol* 5, 18.
- Sezgin E, Levental I, Mayor S, Eggeling C (2017). The mystery of membrane organization: composition, regulation and roles of lipid rafts. *Nat Rev Mol Cell Biol* 18, 361–374.
- Shao B, Yago T, Setiadi H, Wang Y, Mehta-D'souza P, Fu J, Crocker PR, Rodgers W, Xia L, McEver RP (2015). O-glycans direct selectin ligands to lipid rafts on leukocytes. *Proc Natl Acad Sci USA* 112, 8661–8666.
- Sharma P, Varma R, Sarasij RC, Ira, Gousset K, Krishnamoorthy, G, Rao M, Mayor S (2004). Nanoscale organization of multiple GPI-anchored proteins in living cell membranes. *Cell* 116, 577–589.
- Shibata AC, Fujiwara TK, Chen L, Suzuki KG, Ishikawa Y, Nemoto YL, Miwa Y, Kalay Z, Chadda R, Naruse K, et al. (2012). Archipelago architecture of the focal adhesion: membrane molecules freely enter and exit from the focal adhesion zone. *Cytoskeleton (Hoboken)* 69, 380–392.
- Shyjan, AM, Heldin P, Butcher EC, Yoshino T, Briskin MJ (1996). Functional cloning of the cDNA for a human hyaluronan synthase. *J Biol Chem* 271, 23395–23399.
- Siiskonen H, Oikari S, Pasonen-Seppänen S, Rilla K (2015). Hyaluronan synthase 1: a mysterious enzyme with unexpected functions. *Front Immunol* 6, 43.
- Sinnecker D, Voigt P, Hellwig N, Schaefer M (2005). Reversible photo-bleaching of enhanced green fluorescent proteins. *Biochemistry* 44, 7085–7094.
- Skandalis SS, Kozlova I, Engström U, Hellman U, Heldin P (2010). Proteomic identification of CD44 interacting proteins. *IUBMB Life* 62, 833–840.
- Strale PO, Duchesne L, Peyret G, Montel L, Nguyen T, Png E, Tampé R, Troyanovsky S, Hénon S, Ladoux B, et al. (2015). The formation of ordered nanoclusters controls cadherin anchoring to actin and cell-cell contact fluidity. *J Cell Biol* 210, 333–346.
- Tanaka KA, Suzuki KG, Shirai YM, Shibutani ST, Miyahara MS, Tsuboi H, Yahara M, Yoshimura A, Mayor S, Fujiwara TK, et al. (2010). Membrane molecules mobile even after chemical fixation. *Nat Methods* 7, 865–866.
- Terrillon S, Bouvier M (2004). Roles of G-protein-coupled receptor dimerization. *EMBO Rep* 5, 30–34.
- Thankamony SP, Knudson W (2006). Acylation of CD44 and its association with lipid rafts are required for receptor and hyaluronan endocytosis. *J Biol Chem* 281, 34601–34609.
- Torreno-Pina JA, Castro BM, Manzo C, Buschow SI, Cambi A, Garcia-Parajo MF (2014). Enhanced receptor-clathrin interactions induced by N-glycan-mediated membrane micropatterning. *Proc Natl Acad Sci USA* 111, 11037–11042.
- Totsukawa G, Yamakita Y, Yamashiro S, Hartshorne DJ, Sasaki Y, Matsumura F (2000). Distinct roles of ROCK (Rho-kinase) and MLCK in spatial regulation of MLC phosphorylation for assembly of stress fibers and focal adhesions in 3T3 fibroblasts. *J Cell Biol* 150, 797–806.
- Vachon E, Martin R, Plumb J, Kwok V, Vandivier RW, Glogauer M, Kapus A, Wang X, Chow CW, Grinstein S, et al. (2006). CD44 is a phagocytic receptor. *Blood* 107, 4149–4158.
- van Zanten TS, Mayor S (2015). Current approaches to studying membrane organization. *F1000Research* 4, 1–15.
- Wang Y, Yago T, Zhang N, Abdisalaam S, Alexandrakis G, Rodgers W, McEver RP (2014). Cytoskeletal regulation of CD44 membrane organization and interactions with E-selectin. *J Biol Chem* 289, 35159–35171.
- Yang C, Cao M, Liu H, He Y, Xu J, Du Y, Liu Y, Wang W, Cui L, Hu J, et al. (2012). The high and low molecular weight forms of hyaluronan have distinct effects on CD44 clustering. *J Biol Chem* 287, 43094–43107.
- Zhu D, Bourguignon LY (2000). Interaction between CD44 and the repeat domain of ankyrin promotes hyaluronic acid-mediated ovarian tumor cell migration. *J Cell Physiol* 183, 182–195.